nature communications

Article

https://doi.org/10.1038/s41467-026-69471-4

High-throughput multi-organ proteomics workflow for drug efficacy and toxicity analysis

Received: 22 April 2025

Accepted: 2 February 2026

Published online: 09 February 2026

Check for updates

Yun Xiong[1,2,3,8], Lin Tan[1,2,3,8], Wai-kin Chan[1,3,8], Dandan Zhu[4], Huimin Zhang[4], Eric S. Yin[1,3], Sri Ramya Donepudi[1,5], Jibin Ding[1,2,3], Bo Wei[1,3], Bao Tran[1,3], Sara Martinez[1,3], Iqbal Mahmud[1,3], Faiza Hanif Waghu[1], Hamish I. Stewart[6], Daniel J. Hermanson[6], Rehan Akbani[1,3], John N. Weinstein[1,2,3], Junjie Chen[4] & Philip L. Lorenzi[1,2,3,7]

Rapid and comprehensive analysis of complex proteomes across large sample sets is vital for unlocking the potential of systems biology. We present a high-throughput mass spectrometry (MS) proteomics method that integrates narrow-window data-independent acquisition (nDIA) with short-gradient micro-flow chromatography, enabling profiling of >240 samples per day. This optimized MS approach identifies 6,201 and 7,466 human proteins with 1- and 2-min gradients, respectively. As a practical application, we analyzed 507 samples composed of 13 different tissues from mice treated with the enzyme-drug L-asparaginase (ASNase) or its glutaminase-free Q59L mutant, generating a quantitative profile of 11,472 proteins following drug treatment. The MS results confirmed the impact of ASNase on amino acid metabolism in solid tissues. Further analysis revealed broad suppression of anticoagulants and cholesterol metabolism and uncovered numerous tissue-specific dysregulated pathways. In summary, the optimized high-throughput proteomics method accelerates systems-level analysis of a preclinical model to generate biological insights and clinically actionable hypotheses.

The past decade witnessed remarkable technological and scientific strides that paved the way for advances in systems biology[1,2]. Innovations in genome sequencing have enabled the generation of large molecular datasets spanning a range of biological systems and matrices, from cells to tissues to biological fluids[3,4]. Concurrently, mass spectrometry (MS)-based proteomics has emerged as an essential tool for high-throughput protein-level measurements, becoming indispensable for functional genomics and systems biology[5–7].

MS-based proteomics studies can typically be divided into three major steps: sample preparation, MS data acquisition, and data analysis. Whereas data analysis tools have improved significantly in recent years[8–12], sample pretreatment and MS-based data acquisition remain limiting steps in proteomics investigation. A variety of sample preparation workflows have been developed for proteomic studies with specific sample types and experimental goals[13,14]. However, most workflows are limited in the number of samples that can be processed

[1]Department of Bioinformatics and Computational Biology, The University of Texas MD Anderson Cancer Center (MDACC), Houston, TX, USA. [2]Proteomics Core Facility, Department of Bioinformatics and Computational Biology, The University of Texas MD Anderson Cancer Center (MDACC), Houston, TX, USA. [3]Metabolomics Core Facility, Department of Bioinformatics and Computational Biology, The University of Texas MD Anderson Cancer Center (MDACC), Houston, TX, USA. [4]Department of Experimental Radiation Oncology, The University of Texas MD Anderson Cancer Center, Houston, TX, USA. [5]Department of Pharmacology and Chemical Biology, University of Pittsburgh, Pittsburgh, PA, USA. [6]Thermo Fisher Scientific GmbH, Bremen, Germany. [7]Department of Hematology and Hematopoietic Cell Transplantation, City of Hope National Medical Center, Duarte, CA, USA. [8]These authors contributed equally: Yun Xiong, Lin Tan, Wai-kin Chan. e-mail: plorenzi@coh.org

simultaneously, precluding their application to larger systems biology studies. For MS data acquisition, proteome coverage is a critical challenge due to the wide dynamic range of protein expression levels in cells, ranging from tens to over a million copies per cell. The most common approach to address that complexity has been multi-shot proteomics with offline peptide fractionation[15–17], but this approach necessitates extensive instrument time and large sample volumes. Prompted by those limitations, ongoing effort has been allocated to the development of improved single-shot strategies. Recently, narrow-window DIA (nDIA) was reported to achieve the identification of ~10,000 proteins within 1 h, and ~7000 proteins in a 5-min gradient on the Orbitrap Astral MS[18].

Here, building on recent advances with nDIA, we introduce a workflow that combines an optimized nDIA-MS method with high-throughput sample preparation to facilitate rapid and in-depth proteome profiling. The method employs 1-Th quadrupole isolation windows and achieves identification of 6,201 and 7466 proteins with 1- and 2-min LC gradients, respectively. Our streamlined sample preparation incorporates high-throughput tissue homogenization, adaptive focused acoustics (AFA)-assisted proteolysis, and Evotip-accelerated desalting, enabling the processing of up to 96 tissue samples within 5 h. To demonstrate the utility of our approach, we conducted a systems proteomics analysis of 507 biological samples across 13 tissue types to examine the systems pharmacology of L-Asparaginase (ASNase). The results provided a quantitative landscape of 11,472 proteins, uncovering distinct tissue-specific responses that shed light on mechanisms of ASNase sensitivity, resistance, and toxicity.

Results

Identification of 6,201 proteins per minute with nDIA-MS

The Orbitrap Astral MS system combines a modified Orbitrap Exploris 480 MS with the asymmetric track lossless (Astral) analyzer[19]. The Astral analyzer supports parallel MS2 scanning and achieves MS acquisition rates of up to 200 Hz, making it well suited for high-throughput proteomics analysis[20,21].

As a benchmark for high-throughput analysis, the Evosep One system (Evosep, #AN-024A-500SPD) coupled with a timsTOF Pro 2 identifies 2500 proteins with a 2.2-min LC gradient, achieving a protein identification rate of over 1000 proteins per min (Supplementary Fig. 1a, b). Based on that, we coupled an Evosep One system with an Orbitrap Astral MS (Supplementary Fig. 1c). Using a similar LC gradient and nDIA MS method, we identified an average of 5160 proteins and 34,173 peptides from 200 ng of HeLa digest (Fig. 1a, Supplementary Data 1). To further improve proteome coverage, we modified the LC system by transferring the Evosep endurance column (Evosep, #EV1107, 4 cm × 150 µm, 1.9 µm particle size) and stainless-steel emitter (Evosep, #EV1086, ID 30 µm) to a Vanquish Neo UHPLC system. This modification permitted greater LC gradient flexibility. With an optimized 2-min gradient, proteome coverage was improved to an average of 6549 proteins and 54,306 peptides (Fig. 1a).

Thereafter, we evaluated various MS data acquisition parameters (Supplementary Fig. 1c). Consistent with previous studies[18], decreasing MS2 maximum injection time (IT) from 3.5 ms to 2.5 ms improved peptide detection (Fig. 1b, Supplementary Data 2). Further decreases below 2 ms led to decreased identifications. We next investigated the impact of mass range (MR) on duty cycle, comparing MRs of 380–980, 400–800, and 495–745 Th with corresponding isolation windows (Fig. 1c, Supplementary Data 3). The 495–745 Th MR with a 1 Th isolation window delivered optimal results at the protein level. Further exploration of isolation windows from 0.8 to 2.0 Th confirmed that a 1 Th isolation window yielded the highest number of protein identifications (Fig. 1d, Supplementary Data 4). Automatic gain control (AGC) target values ranging from 100 to 600 produced similar results, with an AGC of 500 marginally improving precursor ion detection (Fig. 1e, Supplementary Data 5). Based on the evaluations, we established a modified nDIA method with an injection time of 2.5 ms, MR of 495–745, 1 Th isolation window, and an AGC value of 500.

We next assessed the performance across LC gradients from 1 to 5 min. Notably, even with a 1-min gradient, we still identified ~6201 human proteins from 1 ug HeLa digest, albeit with a decrease in peptide number (Fig. 1f, Supplementary Data 6). A 2-min gradient yielded 7466 proteins and 59,919 peptides. Proteome coverage remained at nearly 8000 proteins with gradients from 3 to 5 min. The protein identification rate of up to 6201 proteins per min greatly exceeds that of previous reports[22–24] (Supplementary Fig. 1a, b).

To evaluate the quantitative performance of the optimized method, we analyzed proteome samples from three species (human, yeast, and *Escherichia coli*) mixed in various ratios. Overall, an average of 9434 proteins were identified in each mixed sample (Fig. 1g, Supplementary Data 7). Quantitative analysis demonstrated accurate protein quantitation across six different ratios (1:9, 1:4, 2:3, 3:2, 4:1, and 9:1) (Fig. 1h). By comparing the different mixtures, we found that the total MS intensities of yeast and *Escherichia coli peptides* increase linearly with respect to sample input (Fig. 1i).

High-throughput sample preparation accelerates large-scale tissue proteomics

Inspired by previously reported high-throughput workflows[25–27], we implemented a rapid, reproducible, and broadly accessible sample preparation pipeline for large-scale tissue proteomics, integrating high-throughput tissue homogenization, AFA-accelerated proteolysis, and Evotip desalting (Fig. 2a). The Precellys Evolution tissue homogenizer performs bead-based protein extraction for up to 24 samples simultaneously, achieving thorough homogenization in less than 1 min. Protein digestion is accelerated using a Covaris R230 Focused-Ultrasonicator, which can handle 96 samples concurrently. Peptide desalting with racked Evotips enabled simultaneous cleaning of up to 96 peptide samples in 30 min.

We next compared proteolytic digestion performance with and without sonication across durations from 30 min to 15 h (Fig. 2b–d, Supplementary Data 8). MS results showed that 4-h digestion with AFA-assisted sonication provided the highest number of peptides and proteins, although minor differences were observed across conditions (Fig. 2b, c). Over 90% of peptides had only one or no missed cleavage sites across all conditions (Fig. 2d), with AFA-assisted digestion exhibiting slightly better performance in all scenarios. We ultimately chose 4-h digestion to maximize protein recovery, which translates to a total of ~5 h to process 96 samples (Fig. 2a).

We next analyzed three mouse tissues (brain, kidney, and lung) to compare the output obtained from a standard workflow and the optimized high-throughput workflow (Fig. 2e, Supplementary Fig. 1d, and Supplementary Data 9). The high-throughput method identified an average of 6976, 5665, and 6355 proteins from brain, kidney, and lung, respectively, which was comparable to the results from the standard workflow. Pairwise comparisons of protein abundance ratios between two tissues at a time demonstrated Pearson correlation coefficients consistently exceeding 0.83 (Fig. 2f, Supplementary Fig. 1e, f), indicating comparable quantitative performance between the two methods.

We next estimated the sample preparation time required to process 507 tissue samples (Supplementary Fig. 1g, h). The standard workflow requires 369 work hours, equivalent to 46.1 × 8-h workdays. The high-throughput workflow, however, needs only 46.9 work hours (5.9 workdays), providing more than seven times higher throughput for large-scale studies.

Multi-organ quantitative profiling of 11,472 proteins following ASNase treatment

L-Asparaginase (ASNase) is a critical component of the standard of care for pediatric acute lymphoblastic leukemia (ALL). However, its application to adult leukemias and solid tumors is hindered by significant

https://doi.org/10.1038/s41467-026-69471-4

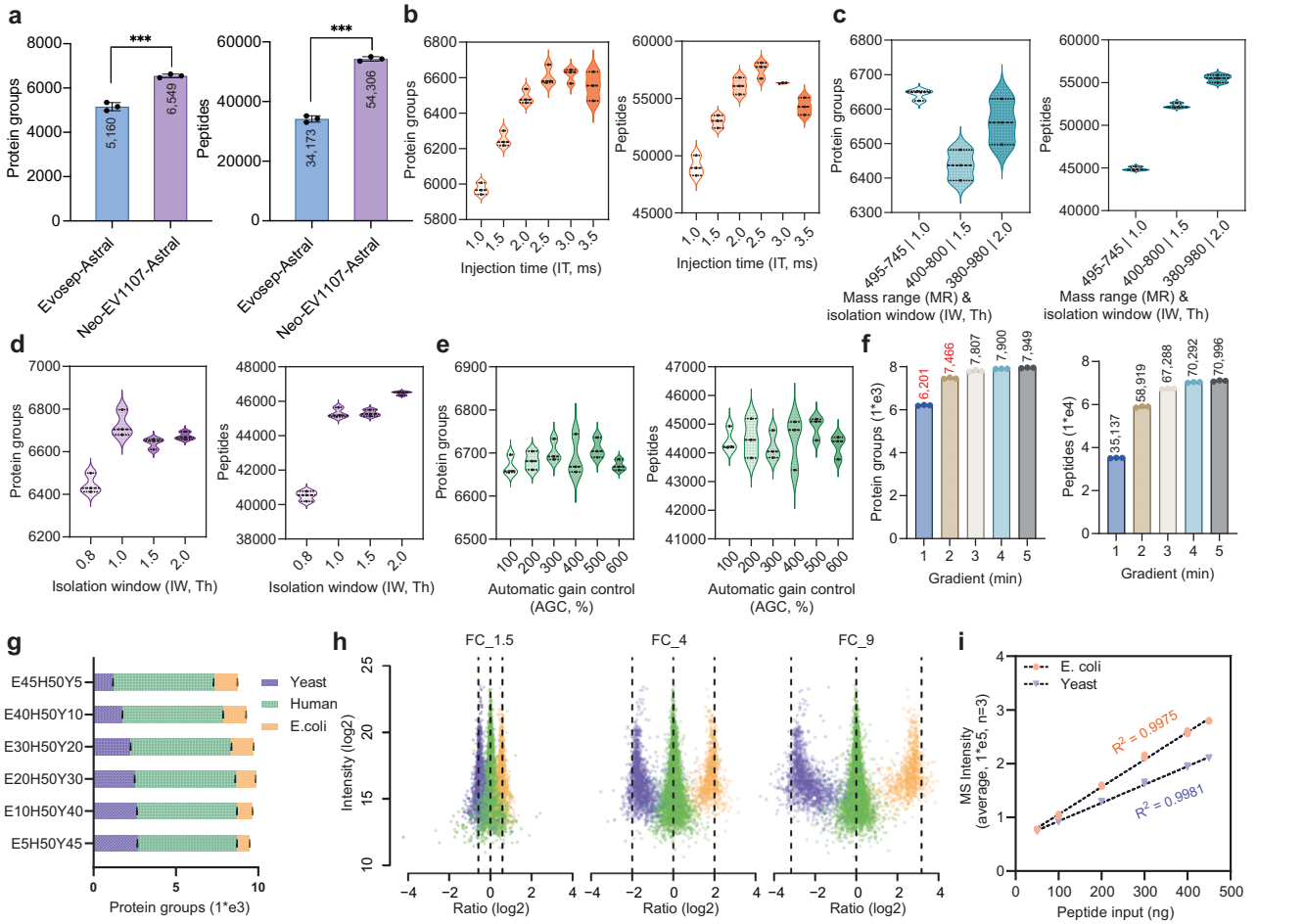

Fig. 1 | High-throughput nDIA enables identification of 6201 proteins with a 1-min LC gradient. a Comparison of the number of identified protein groups and peptides using Evosep-Astral and Neo-Evosep-Astral methods. Statistical analyses for all pairwise comparisons were performed using two-tailed Student's *t* tests. The resulting *p* values were 0.00028 for protein groups and 1.2×10^{-5} for peptides. Significance is indicated as $p < 0.05$ (*), $p < 0.01$ (**), $p < 0.001$ (***), and not significant (ns). No adjustments for multiple comparisons were applied. **b** Comparison of the number of identified protein groups and peptides with indicated maximum injection time (IT) ranging from 1 ms to 3.5 ms. **c** Comparison of the number of identified protein groups and peptides with different combinations of mass range (MR) and isolation window (IW). **d** Comparison of the number of identified protein groups and peptides with MS2 IW ranging from 0.8 Th to 2.0 Th. **e** Comparison of the number of identified protein groups and peptides with automatic gain control (AGC) value ranging from 100 to 600. **f** Number of the identified protein groups and peptides using the refined nDIA method with 1- to 5-min LC gradients. **g** Protein groups identified from mixed samples containing protein digests from *E. coli* (E), human (H), or yeast (Y) in various ratios (E5H50Y45, E10H50Y40, E20H50Y30, E30H50Y20, E40H50Y10 and E45H50Y5). **h** Peptide Ion intensity as a function of ratio for all runs in (**i**). Dashed lines represent expected log2(A/B) values for proteins from humans (green), yeast (purple) and *E. coli* (orange). FC_9, FC_4, and FC_1.5 are calculated from log2(E45H50Y5/E5H50Y45), log2(E40H50Y10/E10H50Y40), and log2(E30H50Y20/E20H50Y30), respectively. **i** Correlation between MS intensity and peptide input for *E. coli* and yeast from runs performed in (**g**). All error bars and scatter points represent $n = 3$ technical replicates from a single HeLa digest sample. Data are presented as mean ± SD. Source data are provided as a Source Data file.

side effects and drug resistance[28]. ASNase toxicity is attributed in part to its glutaminase co-activity[28]. There has been interest in engineering glutaminase-free variants that decrease side effects while maintaining efficacy[29]. We previously demonstrated the anticancer activity of the glutaminase-free Q59L mutant ($ASNase^{Q59L}$) against ASNS-negative cell lines[30–32], but those findings failed to translate to a preclinical mouse model[31], suggesting that ASNase glutaminase activity is necessary for its anticancer efficacy (Fig. 3a). To aid in the development of ASNase-based therapeutic strategies, it is essential to gain a systems-level understanding of the mechanisms through which ASNase mediates anticancer activity and toxicity.

To that end, we applied the optimized method to analyze tissue samples from NSG mice treated with PBS (vehicle control), 20,000 U/kg $ASNase^{WT}$ (Spectrila®), or 20,000 U/kg $ASNase^{Q59L}$ for 0, 1, 3, 5, and 8 days (Fig. 3b). At each time point, mice were euthanized, and 13 tissues were collected, including subcutaneous white adipose tissue (SQWAT), gonadal adipose tissue (GAT), lung, spleen, stomach, small and large intestine, liver, kidney, heart, leg muscle, brain, and bone marrow (Fig. 3c). Analysis of a total of 507 collected tissue samples yielded 11,472 proteins and 104,784 peptides across all samples (Fig. 3d, Supplementary Fig. 1i, and Supplementary Data 10). The highest numbers of proteins and peptides were observed in the brain, followed by the large intestine, stomach, lung, spleen, GAT, bone marrow, and SQWAT. The lowest identifications were found in leg muscle and heart. As anticipated, the correlation matrix displayed strong associations between the two fat depots, SQWAT and GAT (Fig. 3e). Lung protein expression correlated strongly with that of spleen, bone marrow, and kidney. Large intestine protein expression was more strongly correlated with that of stomach than with small intestine (Fig. 3e). Unsupervised clustering using t-SNE confirmed the similarity of stomach and large intestine (Fig. 3f). We then used heatmaps to illustrate the quantitative overview of protein expression following ASNase treatment in each tissue (Fig. 3g). In most organs, we observed significant differences in protein expression between

https://doi.org/10.1038/s41467-026-69471-4

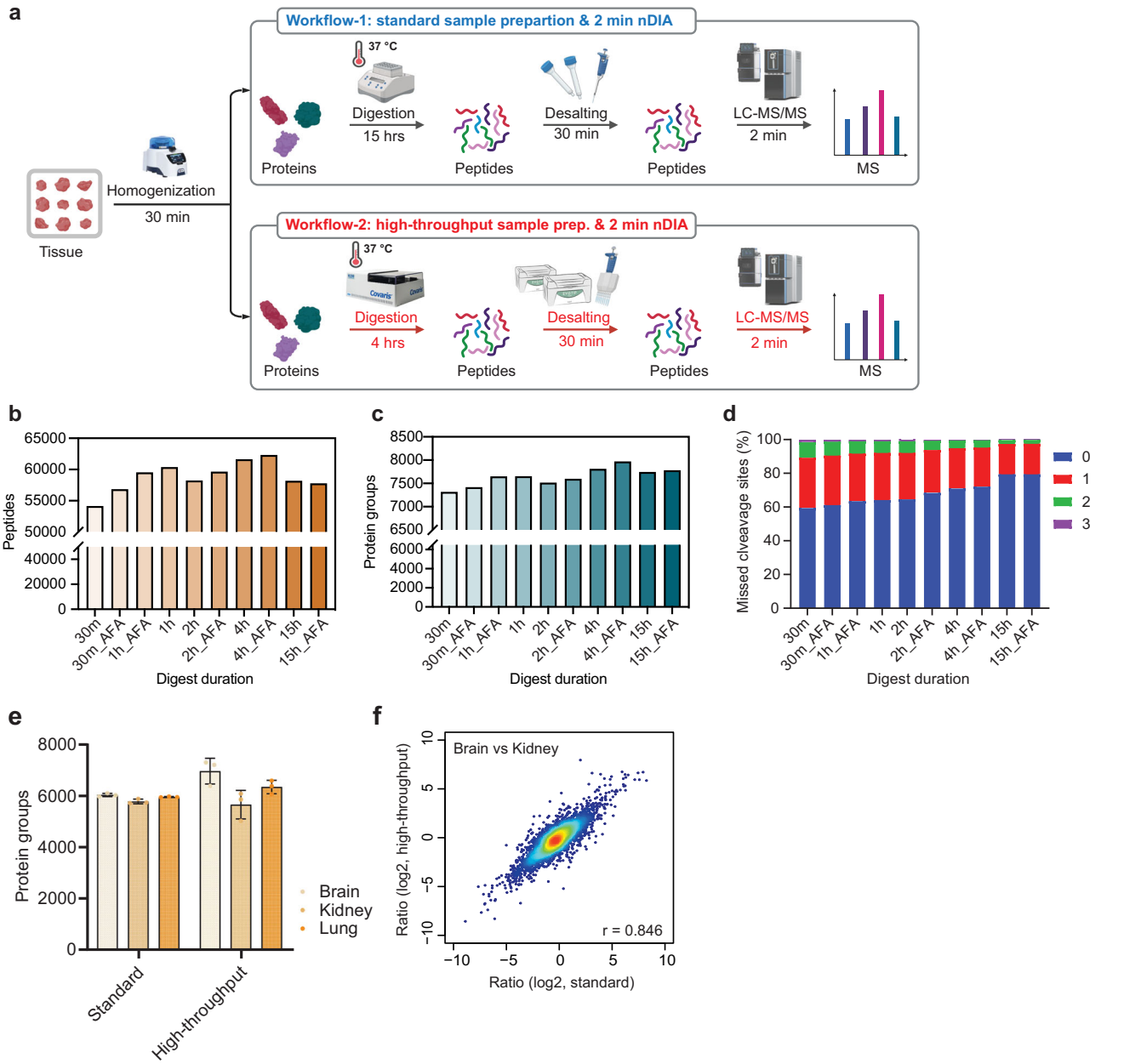

Fig. 2 | High-throughput sample preparation accelerates large-scale tissue proteomics. a Workflows for standard and high-throughput sample preparation for large-scale tissue proteomics. Created in BioRender. Xiong, Y. (2026) https://BioRender.com/j7osk2i. Number of identified peptides (**b**) and proteins groups (**c**) using indicated proteolytic digestion durations with or without adaptive focused acoustics (AFA)-assisted proteolysis. **d** Percentages of identified peptides with 0, 1, 2, or 3 missed cleavage sites for indicated proteolytic digestion durations with or without AFA-assisted proteolysis. **e** Number of identified protein groups with samples prepared from brain, kidney, and lung tissues using the standard and high-throughput workflows. All error bars and scatter points represent $n = 3$ biological replicates from three mice. Data are presented as mean ± SD. **f** Correlation analysis of the pairwise ratios between brain and kidney calculated using the data generated by standard and high-throughput workflows. Source data are provided as a Source Data file.

ASNase^{WT} and PBS treatments, whereas ASNase^{Q59L} yielded only minor differences compared to PBS (Fig. 3g). For example, we saw notable changes in the spleen, but ASNase^{Q59L} also induced unique changes in the bone marrow, kidney, and GAT. These results suggest organ-specific drug effects. We next mined these data to generate insights into the mechanisms of ASNase efficacy and toxicity across different tissues.

Amino acid metabolodynamics in whole blood confirm the efficacy of ASNase

To confirm the efficacy of ASNase^{WT}, we measured the levels of asparagine (ASN) and aspartic acid (ASP) in whole blood samples (Supplementary Fig. 2a). Consistent with our previous results[31,32], ASN reached a trough level after 1 day of treatment with ASNase^{WT} and remained at trough level throughout the 8-day time course, while ASP levels were essentially unaffected (Fig. 4a, b). In contrast, treatment with ASNase^{Q59L} yielded only partial and transient depletion of ASN followed by rapid restoration, suggesting that the body mounted resistance by up-regulating production of ASN.

Our previous studies observed that ASNase^{WT} and ASNase^{Q59L} had subtly different effects on glutamine (GLN) and glutamic acid (GLU) levels in a 24-h time course[31,32]. In this study, the extended 8-d time course revealed significant increases of both GLN and GLU levels

https://doi.org/10.1038/s41467-026-69471-4

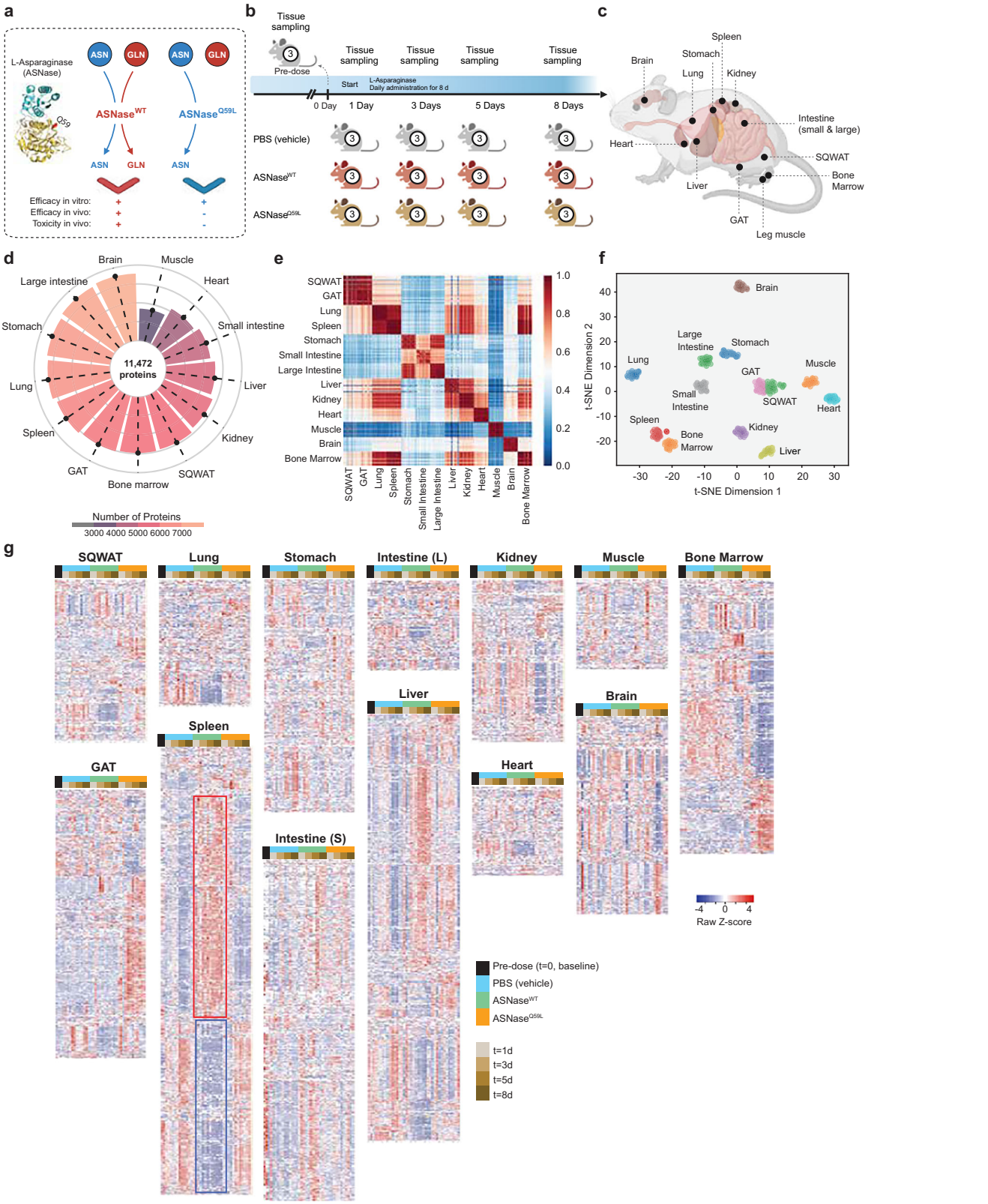

Fig. 3 | Tissue proteomic landscape of ASNase treatment. a Biochemical reactions catalyzed by ASNase^{WT} and ASNase^{Q59L}. **b** Schematic overview of the experimental design. **c** Overview of the mouse tissues collected for mass spectrometry proteomic analysis. **d** Total number of proteins identified in each tissue across all treatment groups. **e** Correlation matrix heatmap of the data generated from 13 mouse tissues. The heatmap was generated using Python. The Pearson correlation coefficient values were calculated based on the MS intensities of each protein in certain samples. **f** Unsupervised clustering of tissue proteomics data via t-SNE. **g** Protein abundance in 13 tissues over an 8-d time course of PBS, ASNase^{WT}, or ASNase^{Q59L} treatments. t, time. Source data are provided as a Source Data file. **a**, **b**, **c** created in BioRender. Xiong, Y. (2026) https://BioRender.com/o2a9ur4.

https://doi.org/10.1038/s41467-026-69471-4

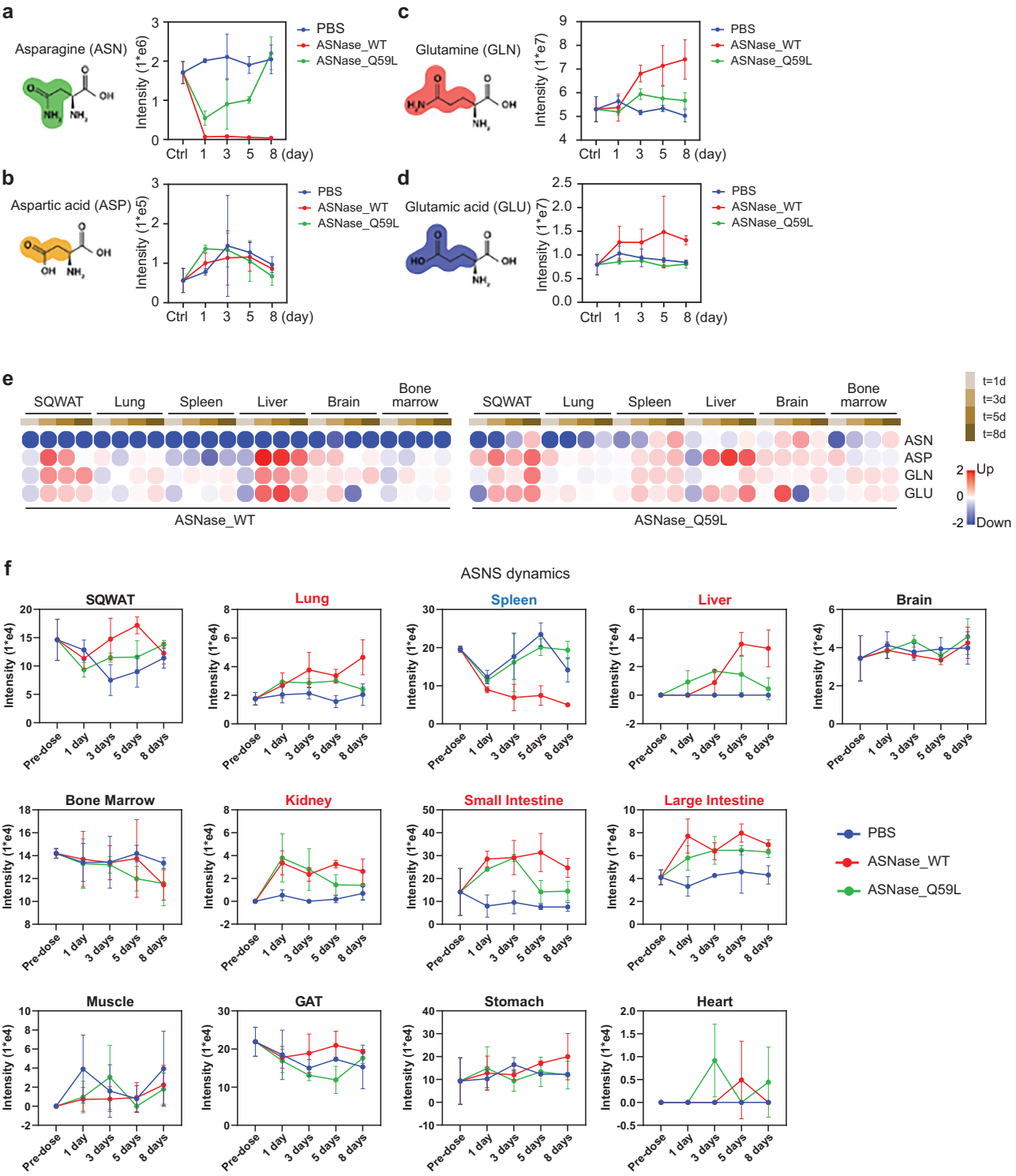

Fig. 4 | Validation of ASNase efficacy on amino acid metabolism. The metabolodynamics of asparagine (ASN) (**a**) aspartic acid (ASP) (**b**) glutamine (GLN) (**c**) and glutamic acid (GLU) (**d**) in blood following either PBS, ASNase^{WT}, or ASNase^{Q59L} treatment. **e** The metabolodynamics of ASN, ASP, GLN, and GLU in the six indicated solid tissues following either PBS, ASNase^{WT}, or ASNase^{Q59L} treatment. **f** The dynamic protein levels of ASNS in thirteen indicated solid tissues following either PBS, ASNase^{WT}, or ASNase^{Q59L} treatment. All error bars and scatter points represent $n = 3$ biological replicates from three mice. Data are presented as mean ± SD. Source data are provided as a Source Data file.

following ASNase^{WT} but not ASNase^{Q59L} treatment (Fig. 4c, d), consistent with the reported up-regulation of glutamine synthetase (GLUL) and glutaminases (GLS, GLS2) following ASNase^{WT} treatment in vitro[33,34]. These data explain the in vivo efficacy of ASNase^{WT} and highlight key differences between ASNase^{WT} and ASNase^{Q59L}.

Organ-specific resistance and vulnerability to ASNase

To assess the system-wide pharmacodynamic and metabolodynamic effects of ASNase in solid tissues, we monitored ASN, ASP, GLN, and GLU levels across six tissues: SQWAT, lung, spleen, liver, brain, and bone marrow (Fig. 4e). Consistent with observations in blood,

ASNase^{WT} treatment resulted in a sustained depletion of ASN in all six tissues, whereas ASNase^{Q59L} initially decreased ASN levels but subsequently up-regulated ASN at these sites (Fig. 4e). We did not observe significant changes in ASP, GLN, or GLU levels after drug treatment in most tissues, except in the liver, where ASNase^{WT} induced increases in all three amino acids after prolonged treatment. Notably, we observed a decrease in ASP levels in the spleen following ASNase^{WT} but not ASNase^{Q59L} treatment. These findings contrast with the observed blood effects, highlighting spleen-specific suppression of ASP metabolism as a targeted vulnerability of ASNase^{WT} treatment.

Asparagine synthetase (ASNS) is a well-established mediator of resistance to ASNase[28,30,31,35,36]. However, multiple reports have also described ASNS-low cancer cells exhibiting resistance to ASNase in vivo[31,37,38]. In assessing ASNS expression levels we observed rapid and extensive up-regulation in the lung, small intestine, large intestine, liver, and kidney following both ASNase^{WT} and ASNase^{Q59L} treatments (Fig. 4f), suggesting that broad ASNS up-regulation could potentially explain the resistance of low-ASNS tumors to ASNase treatment. In contrast, both ASNase variants suppressed ASNS up-regulation in brain, bone marrow, heart, and muscle. Strikingly, only spleen exhibited down-regulation of ASNS following ASNase^{WT} but not ASNase^{Q59L} treatment.

We also examined the effects of ASNase on the broad network of proteins associated with ASN, ASP, GLN, and GLU metabolism (Supplementary Fig. 2b, c). Many of the observed changes suggested adaptive responses (i.e., drug resistance-associated responses) to ASNase^{WT}. Specifically, several proteins were consistently up- or down-regulated across multiple tissues. For instance, GLUL was upregulated in spleen, stomach, small intestine, kidney, and heart; GLS was upregulated in SQWAT, lung, spleen, stomach, small intestine, and kidney; GLUD1 was upregulated in spleen, stomach, and bone marrow; at least one transaminase (GOT1, GOT2, GPT, GPT2) were upregulated in all 13 tissues; at least one glutamine transporter (SLC1A5, SLC38A3) were upregulated in stomach, and liver; and at least one glutathione metabolism component (GCLC, GCLM) were upregulated in SQWAT, GAT, small intestine, large intestine, brain, and bone marrow. CPQ and GOT2 were down-regulated in SQWAT, liver, and muscle.

Conversely, several organs exhibited tissue-specific modulation of glutamine metabolism-related proteins in response to ASNase^{WT} treatment (Supplementary Fig. 2b, c). For instance, SQWAT exhibited down-regulation of FOLH1, GOT1, and SLC25A22. Spleen exhibited down-regulation of ALDH18A1, CAD, CTPS1, DARS2, GCLM, GMPS, PAICS, PFAS, PPAT, and SLC1A5. Liver exhibited down-regulation of ABAT, GGCX, GLS, GLS2, GLUL, and NADSYN1. Kidney exhibited down-regulation of ACY1, ACY3, BCAT1, CAD, CTPS1, GATB, GCLC, GPT, and SLC25A22. And muscle exhibited down-regulation of ABAT, ASNS, ASPA, ASS1, BCAT2, CAD, DARS2, GCLC, GCLM, GLS, GLUD1, GMPS, GOT1, GPT, NARS2, OPLAH, PAICS, PFAS, SLC1A5, and SLC25A22.

In response to ASNase^{Q59L} treatment, ASPH was upregulated in large intestine, liver, and heart. ASS1 was upregulated in brain and bone marrow. GLS was upregulated in SQWAT, GAT, and bone marrow. GLUD1 was upregulated in liver, brain, and bone marrow. GPT was upregulated in small intestine, liver, and bone marrow. Other tissue-specific regulation includes upregulation of ALDH18A1 in lung, upregulation of NARS2 in stomach, upregulation of CAD, EARS2, GOT1, GPT in small intestine, upregulation of AASS, ASPH, GPT2 in liver, downregulation of AADAT, AASS, ABAT, ACY1, ACY3, ASS1, BCAT1 in kidney, downregulation of GCLC, GLS in muscle, upregulation of GAD2, SLC1A6 in brain, upregulation of GOT1 in bone marrow. Effects that are concordant between ASNase^{WT} and ASNase^{Q59L} (e.g., downregulation of GCLC and GLS in muscle) may be necessary but not sufficient for anticancer activity, whereas effects that are discordant between ASNase^{WT} and ASNase^{Q59L} may suggest mechanistic features associated with anticancer activity versus resistance. For example, upregulation of GLS in bone marrow following ASNase^{Q59L} but not ASNase^{WT} treatment suggests that upregulation of GLS in bone marrow is associated with resistance to ASNase^{Q59L} and/or that suppression of GLS upregulation in bone marrow is associated with sensitivity to ASNase^{WT}.

While the majority of ASNase^{Q59L}-induced protein changes were distinct from those induced by ASNase^{WT}, PSAT1 was a notable exception, showing consistent upregulation in response to both isoforms in the small intestine, large intestine, liver, and kidney.

Overall, these analyses indicate that most organ sites mount an adaptive response to ASNase^{WT} (i.e., upregulate pathways to counteract the resulting nutrient stress). Nevertheless, potentially vulnerable organs (defined as organs unable to upregulate asparagine or glutamine metabolic pathways) included spleen, SQWAT, liver, kidney, and muscle (Fig. 4f). Among those, spleen uniquely exhibited suppression of ASNS protein (Fig. 4f). No clinical toxicities of ASNase have been associated specifically with spleen, muscle, or kidney, suggesting that using ASNase to treat tumors arising from or supported by those tissues may be safe. Liver and SQWAT were vulnerable organs that have been linked to clinical toxicities.

System-wide suppression of anticoagulants and cholesterol metabolism as likely drivers of ASNase toxicity

To explore other coordinated stress responses following drug treatment across tissues, we next compared protein expression profiles between ASNase-treated and PBS-treated samples at the pathway level. Proteins with an average fold change in expression greater than 2 or less than 0.5 and a $p < 0.05$ were classified as differentially modulated (Fig. 5a–d, Supplementary Figs. 3–15, Supplementary Data 11). ASNase^{WT} treatment significantly modulated (positively or negatively) the vast majority of proteins in liver and spleen (Fig. 5a, b). ASNase^{Q59L} treatment mainly up-regulated proteins in the liver, GAT, and small intestine, while down-regulating proteins in kidney, bone marrow, stomach, liver, and brain (Fig. 5c, d).

KEGG pathway enrichment analysis provided several notable insights (Supplementary Figs. 3–15, Supplementary Data 12–24). The suppressive effects of ASNase^{WT} were highly consistent across organ sites, with pathways such as “complement and coagulation cascades,” cholesterol metabolism, and coronavirus disease being nearly uniformly downregulated in all tissues (Fig. 5e). No pathways were uniformly up-regulated across all tissues (Fig. 5e), indicating that the up-regulated pathways are highly tissue-specific. Similarly, ASNase^{Q59L} also did not uniformly modulate any pathways across organ sites (Fig. 5f).

Closer inspection of the MS proteomic data confirmed that most identified proteins in the complement and coagulation cascade and cholesterol metabolism pathways were down-regulated across all 13 tissue types following ASNase^{WT} but not ASNase^{Q59L} treatment (Fig. 6a). Focusing on proteins that were consistently dysregulated across multiple tissues, 28 proteins were commonly up-regulated, and 68 proteins were commonly down-regulated across at least three tissues following ASNase^{WT} treatment (Fig. 6b, c, Supplementary Data 25). ASNase^{Q59L} treatment up- or down-regulated 56 and 24 shared proteins, respectively (Fig. 6d, e). Around 50% of all proteins commonly down-regulated by ASNase^{WT} were involved in cholesterol metabolism or the complement and coagulation cascades (Supplementary Fig. 16a–c). Together, these results suggested that well-known ASNase toxicities—hypertriglyceridemia and venous thromboembolism (VTE)—result from system-wide down-regulation of cholesterol metabolism and the complement and coagulation pathways.

ASNase^{WT} modulation of metabolites and proteins converge on inhibition of DNA replication and activation of ferroptosis in spleen

Although down-regulation of cholesterol metabolism and the complement and coagulation pathways was observed in nearly all tissues

https://doi.org/10.1038/s41467-026-69471-4

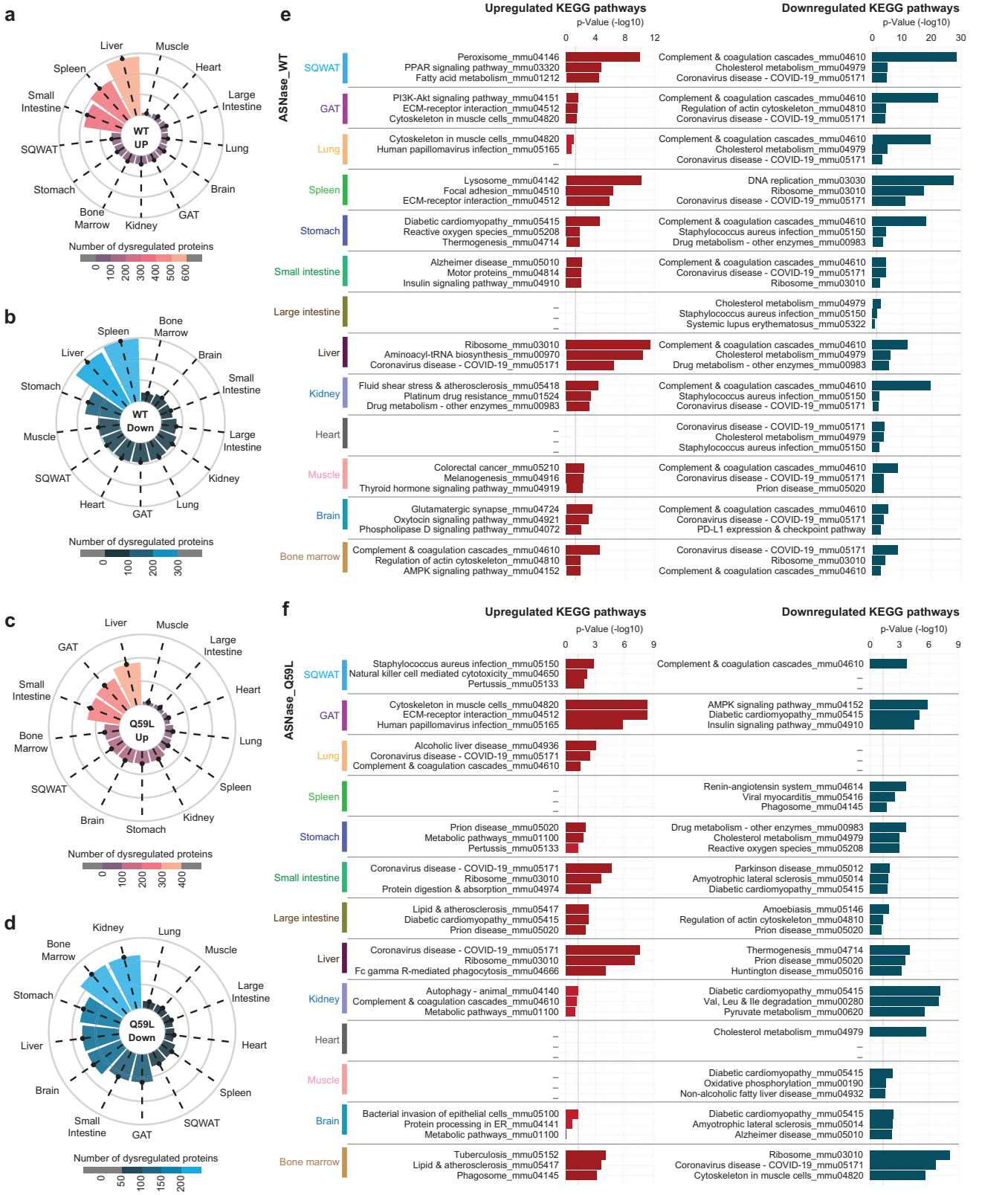

tested, this was not the case in the spleen (Fig. 5e). As noted previously, spleen uniquely exhibited decreased ASP levels (Fig. 4e) and decreased ASNS protein levels following ASNase^{WT} treatment (Fig. 4f). Considering the strong association between spleen and blood cells, we next analyzed the quantitative MS proteome profiles of the spleen following drug treatment. We compared PBS- and ASNase^{WT}-treated spleen proteomes and subjected differentially modulated proteins with a $p < 0.05$ and fold change >2 or <0.5 to functional clustering against the KEGG pathways database (Fig. 7a–c)[39]. Since no dysregulated pathways were enriched prior to 3 days of treatment, we focused on effects at 3, 5, and 8 days. Notably, proteins associated with the "lysosome" pathway were significantly up-regulated at all time points, and DNA replication was significantly down-regulated at all time points (Fig.7a–c). At 8 d, "glutathione metabolism" and "ferroptosis" were significantly up-

https://doi.org/10.1038/s41467-026-69471-4

Fig. 5 | Statistical overview and KEGG pathway enrichment analysis of proteins modulated by ASNase treatment. a Protein expression levels following ASNase^{WT} treatment were compared with PBS-treated controls. Proteins with a fold change greater than 2 and a *p* value less than 0.05 were classified as up-regulated. Data from all the time points (1 d, 3 d, 5 d, and 8 d) were grouped together. **b** Same as (**a**) except proteins with a fold change less than 0.5 and a *p* value less than 0.05 were classified as down-regulated. **c** Same as (**a**) except ASNase^{Q59L} compared to PBS treatment. **d** Same as (**b**) except ASNase^{Q59L} compared to PBS treatment. Statistical analyses for all pairwise comparisons were performed using two-tailed Student's *t* tests. No adjustments for multiple comparisons were applied. **e** KEGG pathway analysis of the up- or down-regulated proteins following ASNase^{WT} treatment in the indicated tissues. **f** Same as (**e**) except ASNase^{Q59L} treatment. Enrichment analysis was performed using DAVID with default settings. *P* values were calculated using the modified Fisher's exact test (EASE score). No adjustments for multiple comparisons were applied. Source data are provided as a Source Data file.

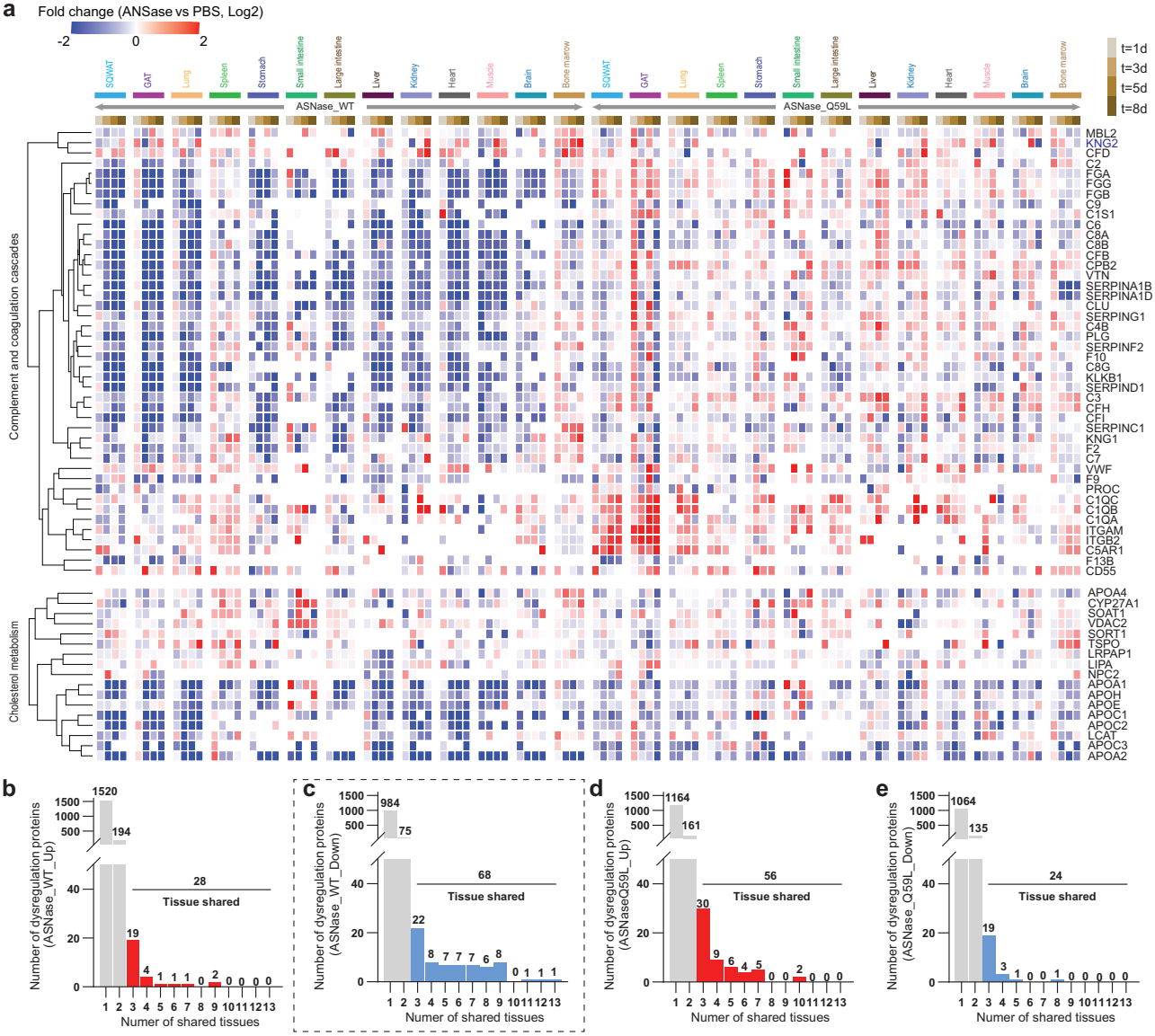

Fig. 6 | ASNase dysregulates a common set of proteins across multiple tissue types. a Heatmap overview of the dynamic protein levels change of proteins involved in the complement and coagulation cascades (top) and the cholesterol metabolism pathway (bottom) following ASNase^{WT} or ASNase^{Q59L} treatment across all the tested tissues. Protein expression levels following ASNase^{WT} or ASNase^{Q59L} treatment were compared to PBS-treated controls, with the Log2 fold change values presented. **b**–**e** Statistical summary of the dysregulated proteins that were common in certain number of tissues. Dysregulation proteins were filtered with a $p < 0.05$ and fold change >2 or <0.5. Proteins commonly dysregulated in at least three tissues were colored in red (up-regulation) or blue (down-regulation). Statistical analyses for all pairwise comparisons were performed using two-tailed Student's *t* tests. No adjustments for multiple comparisons were applied. Source data are provided as a Source Data file.

regulated (Fig. 7c). ASNase^{Q59L} did not affect those pathways (Supplementary Fig. 5).

Consistent with previous reports of ASNase-induced autophagy (a lysosome-driven process)[40], our data showed up-regulation of: (i) lysosomal cysteine proteases CTSA, CTSB, CTSD, CTSF, and CTSZ; (ii) lysosomal glycosidases GLA, GLB1, GNS, GUSB, HEXB, and NAGA; and (iii) lysosomal phosphatases ACP2 and ACP5 following treatment of ASNase^{WT} (Fig. 7d). ASNase^{Q59L} did not significantly modulate lysosomal proteins. The induction of lysosomal proteins may be a consequence of decreased ASP and ASN, since lysosome-driven autophagy plays an important role in producing amino acids via recycling of proteins[41].

https://doi.org/10.1038/s41467-026-69471-4

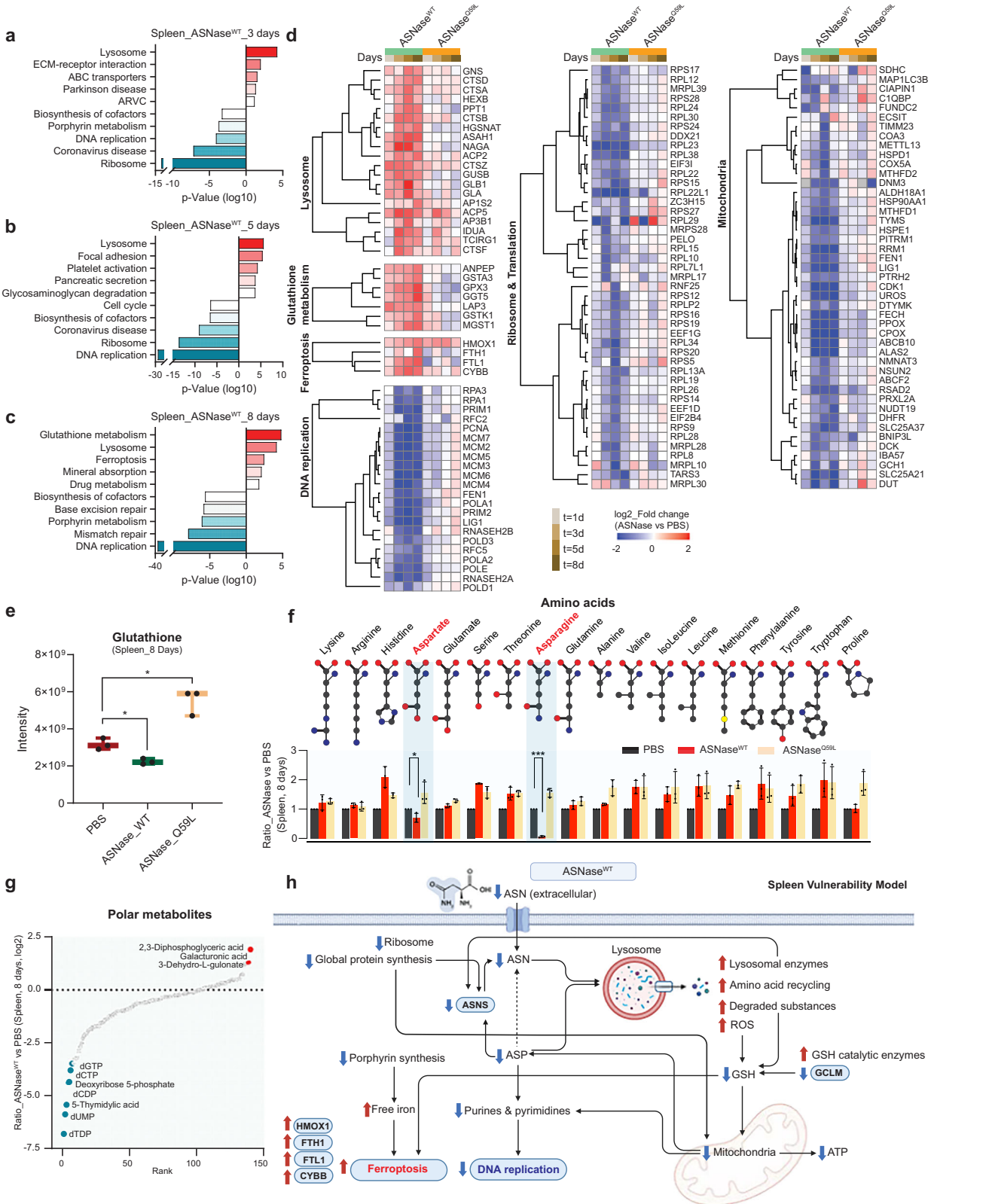

Prolonged ASNase^{WT} treatment also up-regulated glutathione (GSH) metabolism and ferroptosis (Fig. 7c). In parallel, our metabolomic data revealed that GSH was decreased by ASNase^{WT} and significantly increased by ASNase^{Q59L} in the spleen (Fig. 7e). Most up-regulated GSH metabolism proteins were catalytic enzymes (Fig. 7d), including glutathione peroxidase 3 (GPX3), glutathione hydrolase 5 heavy chain (GGT5), and glutathione transferases (GSTA3, GSTK1, and MGST1). Their up-regulation following ASNase^{WT} treatment was consistent with the decrease of GSH level (Fig. 7e). Since GSH is a key reducing equivalent and negative modulator of ferroptosis, its concurrent down-regulation with the up-regulation of ferroptosis was mechanistically consistent[42]. The up-regulated ferroptosis pathway encompassed four proteins including CYBB, FTH1, FTL1, and HMOX1 (Fig. 7d). We also observed down-regulation of porphyrin metabolism

Fig. 7 | Modulation of the spleen proteome by ASNase. KEGG pathway analysis of the upregulated or downregulated proteins following 3 days (**a**) 5 days (**b**) and 8 days (**c**) ASNase^{WT} treatment in the spleen. Enrichment analysis was performed using DAVID with default settings. *P* values were calculated using the modified Fisher's exact test (EASE score). No adjustments for multiple comparisons were applied. **d** Heatmap overview of the dynamic protein levels change of proteins involved in lysosome, glutathione metabolism, ferroptosis, DNA replication, ribosome and translation, and mitochondria following ASNase^{WT} or ASNase^{Q59L} treatment across all the tested tissues. Protein expression levels following ASNase^{WT} or ASNase^{Q59L} treatment were compared to PBS-treated controls, with the Log2 fold change values presented. **e** Glutathione levels in spleen samples from mice treated with PBS, ASNase^{WT}, or ASNase^{Q59L} for 8 d. Pairwise comparisons against PBS-treated samples revealed statistically significant differences for ASNase^{WT} ($p = 0.019$) and ASNase^{Q59L} ($p = 0.016$). **f** The dynamic regulation of indicated amino acid levels following 8 days treatment with ASNase^{WT} or ASNase^{Q59L} treatment in the spleen. Pairwise comparisons between ASNase^{WT} and PBS-treated samples showed $p = 0.027$ (aspartic acid) and 6.3×10^{-7} (asparagine). **g** Polar metabolite levels in spleen samples from mice treated with ASNase^{WT} for 8 days. **h** Model of spleen vulnerability to ASNase^{WT} treatment. Created in BioRender. Xiong, Y. (2026) https://BioRender.com/cu8cxj0. All error bars and scatter points represent $n = 3$ biological replicates from three mice. Data are presented as mean ± SD. Statistical analyses for all pairwise comparisons were performed using two-tailed Student's *t* tests. Significance is indicated as $p < 0.05$ (*), $p < 0.01$ (**), $p < 0.001$ (***), and not significant (ns). No adjustments for multiple comparisons were applied. Source data are provided as a Source Data file.

following ASNase^{WT} for 3 and 8 days (Fig. 7a, c), prompting the hypothesis that down-regulation of porphyrin metabolism permits accumulation of free iron, which is required for ferroptosis (Fig. 7c).

A number of DNA replication proteins were down-regulated by ASNase^{WT} treatment (Fig. 7a–d): (a) DNA polymerases POLA1, POLA2, POLD1, POLD3, and POLE; (b) components of the MCM2-7 complex MCM2, MCM3, MCM4, MCM5, MCM6, and MCM7; (c) DNA primases PRIM1 and PRIM2; (d) ribonuclease H2 subunits RNASEH2A and RNASEH2B; and (e) other DNA replication-associated proteins PCNA, RPA1/3, RFC2/5, FEN1, and LIG1 (Fig. 7d). Down-regulation of DNA replication may be associated with the decrease of ASP (Fig. 4e), which contributes to de novo synthesis of purine and pyrimidine nucleotides[43]. Interestingly, of all amino acids in spleen following ASNase treatment, only ASP and ASN were clearly down-regulated (Fig. 7f, Supplementary Fig. 17, Supplementary Data 26). Correspondingly, metabolomics indicated significant decrease of several deoxyribonucleotides, including dTDP, dUMP, dTMP, dCDP, dCTP, and dGTP (Fig. 7g, Supplementary Data 27), further supporting the observed down-regulation of nucleotide synthesis at the protein and pathway levels.

Spleen-specific down-regulation of ASNS may be associated with up-regulation of aminopeptidases LAP3 and ANPEP (Fig. 7d) and down-regulation of ribosome and translation pathways (Fig. 7a, b, d, Supplementary Fig 18a, b). A number of mitochondrial proteins that were specifically down-regulated in spleen (Fig. 7d, Supplementary Fig. 18a, b), which is consistent with previous reports that mitochondrial electron transport chain enables synthesis of ASP[44]. To note, in addition to the deoxyribonucleotides that described above, adenosine triphosphate (ATP) was also decreased in spleen following ASNase^{WT} treatment (Supplementary Fig. 18c).

Collectively, integrated analysis of proteomic and metabolomic data implicates the spleen as a highly vulnerable target of ASNase^{WT}. That vulnerability is potentially explained by signaling cascades that modulate amino acid metabolism, energy metabolism, redox metabolism, and global protein synthesis converging on inhibition of DNA replication and induction of cell death (ferroptosis) (Fig. 7h), suggesting a plausible mechanism supported by our findings: (1) ASNase^{WT} decreases ASN and ASP in spleen (Fig. 7f, Supplementary Fig. 17); (2) endoplasmic reticulum stress and protein misfolding are up-regulated[45,46]; (3) lysosomal enzymes are activated (Fig. 7d); (4) reactive oxygen species (ROS) accumulate; (5) GSH is consumed (Fig. 7d, e); (6) damaged mitochondria accumulate; (7) mitophagy clears damaged mitochondria (Fig. 7d) and further decreases ASP production and nucleotide synthesis (Fig. 7f, g) and ATP levels (Supplementary Fig 17c); (8) DNA replication is suppressed (Fig. 7a–d); (9) recycling of damaged RBCs together with suppression of porphyrin synthesis leads to accumulation of free iron (Fig. 7a, c); and (10) ferroptosis is activated (Fig. 7c, d). The observed decrease of ASNS expression is likely due to the combined impairment of protein synthesis (Fig. 7d), decrease of ASP (substrate of ASNS) availability (Fig. 7f), and increased lysosomal degradation (Fig. 7d).

ASNase dysregulates system-wide and tissue-specific pathways

In addition to findings in spleen, our analysis revealed numerous tissue-specific dysregulated pathways in other tissues following ASNase treatment. These observations offer further insights into the effects of ASNase^{WT} at the system-wide and tissue-specific levels. Those results are discussed in the Supplementary Information.

In Vivo Evidence Supporting Proteomic Signatures

To validate key MS proteomic findings, we performed complementary in vivo assays. In brief, three groups of mice ($n = 3$ per group) were treated with[1] vehicle[2], 20,000 IU/kg ASNase, or[3] 20,000 IU/kg ASNase plus 10 mg/kg liproxstatin-1, a ferroptosis inhibitor. Spleen tissue samples were collected on day 8. We measured malondialdehyde (MDA) levels, a widely used marker of lipid peroxidation. ASNase significantly increased MDA levels compared to vehicle. Co-treatment with liproxstatin-1 did not result in a statistically significant reduction in MDA levels (Fig. 8a). These results suggest that ASNase can induce lipid peroxidation in the spleen, which is consistent with the up-regulated glutathione metabolism observed with our proteomics and metabolomics results. The limited sample size and partial pharmacological rescue preclude definitive mechanistic conclusions regarding ferroptosis, but the MDA results and MS proteomics results were consistent directionally.

Blood samples from vehicle- or drug-treated mice were also collected for comprehensive hematological screening. Platelet counts and mean platelet volume did not show statistically significant differences between treatment groups (Fig. 8b, c and Supplementary Fig. 22).

These in vivo assays were included as illustrative examples of how a multi-organ proteomics framework can nominate candidate physiological processes for subsequent targeted investigation.

Discussion

MS-based proteomics has become an essential tool for high-throughput investigation of cellular proteins. While RNA sequencing technologies are adept at quantifying gene expression levels, the direct analysis of proteins—the principal executors of cellular functions—remains indispensable in biological research.

To improve upon the latest advances of high-throughput LC (Evosep, #AN-024A-500SPD) and MS (nDIA on Orbitrap Astral MS[18]) technologies, we present a LC-MS approach that integrates optimized nDIA with short-gradient micro-flow chromatography, yielding identification of 6201 and 7466 proteins with 1- or 2-min LC gradients, respectively. The achieved protein identification rate of up to 6201 proteins per min represents more than a two-fold improvement over previously reported cutting-edge methods (Supplementary Fig. 1b, c)[18,22–24].

The choice of isolation window in nDIA can influence peptide and protein identifications. In our benchmarking, a 1-Th window slightly favored protein-level identification, whereas wider windows (e.g., 2-Th) increased peptide coverage. While the 1-Th window was selected to

https://doi.org/10.1038/s41467-026-69471-4

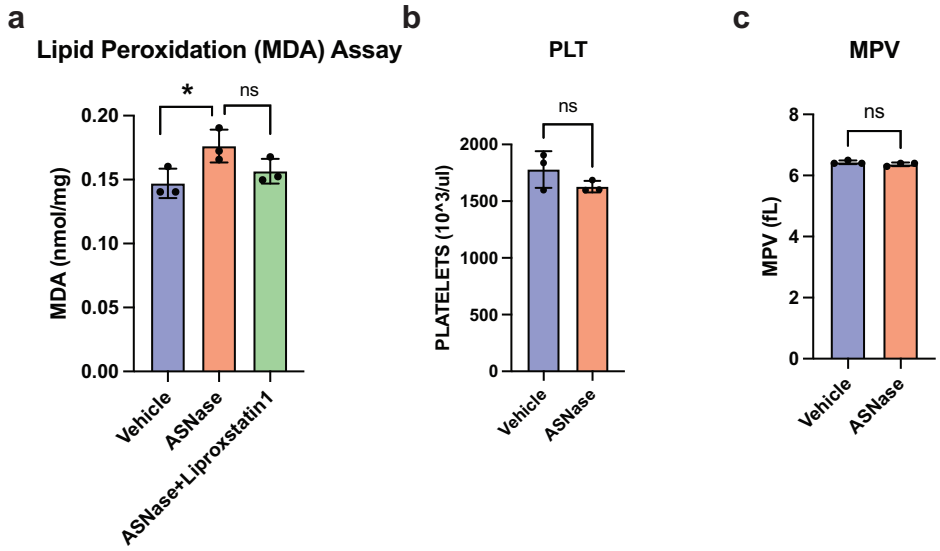

Fig. 8 | In vivo validation of MS proteomic observations. a The change of lipid peroxidation in spleens after a single treatment with vehicle, ASNase alone, or ASNase in combination with liproxstatin-1. The Lipid Peroxidation (MDA) Assay Kit (Abcam, Cat. No. ab118970) was used for the measurement of malondialdehyde (MDA), a widely used marker of lipid peroxidation. Three biological replicates and three technical replicates were included for each treatment condition. Pairwise comparisons yielded $p = 0.043$ for ASNase versus vehicle and $p = 0.10$ for ASNase plus liproxstatin-1 versus ASNase alone. Hematology analyses showing the effect of ASNase treatment on (**b**) platelet counts (PLT) and (**c**) mean platelet volume (MPV). Statistical analyses for all pairwise comparisons were performed using a two-tailed Student's *t* test. "*" denotes $p < 0.05$, "**" denotes $p < 0.01$, and "ns" indicates not significant. All error bars and scatter points represent $n = 3$ biological replicates from three mice. Data are presented as mean ± SD. Source data are provided as a Source Data file.

maximize proteome depth in this discovery-phase study, optimal window size may vary depending on study objectives, such as peptide-level analyses, post-translational modifications, or low-input samples. This highlights the trade-offs between protein coverage and peptide resolution inherent in DIA-based workflows. With our current LC-MS configuration (Thermo Fisher Scientific Vanquish Neo coupled to Orbitrap Astral), although with 1–2 min LC gradients, the full cycle time per sample remains ~6 min, primarily due to LC switching and auto-sampler overhead. As a result, the actual throughput achieved was ~240 samples per day.

Sample preparation also represents a critical rate-limiting step for large-scale proteomics experiments. The rapid tissue proteomics workflow established in this study allows processing up to 96 tissue samples within 5 h, including a 4-h proteolysis step. We used the workflow to obtain more than seven-fold increased throughput in a multi-organ systems proteomics project involving 507 tissue samples (Supplementary Fig. 1h). Decreasing the protein digestion time to 30 min increases overall processing speed to 96 samples per hour but results in a marginal decrease (2.2%) in protein identification (Supplementary Data 8). Our chosen application was tissue proteomics, but the workflow can be adapted to other biological matrices. Future work could integrate this workflow with automated liquid handling to further accelerate sample processing and enhance reproducibility. To further evaluate potential biases, we compared protein identification between the high-throughput and standard workflows across brain, kidney, and lung. Both workflows yielded highly comparable proteome coverage, with >75% of proteins shared (Supplementary Fig. 21). Further analysis of proteins uniquely identified by each workflow revealed no significant differences in physicochemical properties, indicating that the high-throughput workflow does not introduce systematic biases.

We ultimately aimed to test the hypothesis that a preclinical model system combined with a systems-level analysis and our high throughput proteomic profiling workflow would provide clinically relevant insights. We chose the systems pharmacology of ASNase as an application primarily because its toxicity has prevented use for adult patients and cancers beyond pediatric ALL[28]. Additionally, despite >50 years of research, the effects of its glutaminase activity and the mechanistic underpinnings of ASNase sensitivity and resistance are poorly understood. The chosen preclinical model was NSG (NOD-scid IL2Rγnull) mice, which are used widely in leukemia research for their ability to support human cell engraftment. This model allows the study of ASNase-induced metabolic and proteomic changes in the absence of immune rejection. It should be noted, however, that the lack of a functional immune system may influence the observed responses, and studies in immunocompetent models would be expected to provide complementary insights into immune-related effects.

The quantitative profile of 11,472 proteins provides a detailed multi-organ roadmap of dysregulated cellular pathways following ASNase treatment. To assess whether the workflow generates accurate clinical insights, we focused on linking our results to clinically observed toxicities of ASNase—venous thromboembolisms (VTE) and hypertriglyceridemia. Indeed, the observed suppression of the complement and coagulation system has clear mechanistic links to VTE, and the observed suppression of cholesterol metabolism has clear links to hypertriglyceridemia, suggesting that the workflow provides clinically accurate insights.

The complement and coagulation pathways are crucial for host defense against pathogen infection and injury, involving blood-based defense systems that are proteolytically activated to produce active molecules crucial for immunity and clotting[47]. Genes associated with the coronavirus disease pathway also include complement factors and immune response elements. Within the 44 down-regulated proteins associated with the complement and coagulation cascades, 11 have anti-coagulant function (CPB2, KNG1, KNG2, PLG, PROC, SERPINA1B, SERPINA1D, SERPINC1, SERPIND1, SERPINF2, SPERING1), and the remaining 33 have pro-coagulant function. Most of the 11 anti-coagulant proteins were down-regulated in up to 9 of the 13 tissue types (Fig. 6a). In agreement with our results, previous research on the VTE side effects of ASNase identified down-regulation of plasminogen (PLG), antithrombin III (SERPINC1), and fibrinogen (FGA, FGB, FGG)[48,49]. SERPINC1 is of primary interest in current clinical practice; guidance recommends weekly monitoring of SERPINC1 levels in patients and administration of recombinant SERPINC1 when levels fall below 60%

with a repletion target of 80% to 120%[50]. Our findings reveal that SERPINC1 was widely down-regulated in most of the 13 tissues (Fig. 6a) and exhibited a significant decrease in three specific tissues including stomach, liver, and kidney (Supplementary Fig. 16b). Additionally, PLG, SERPINA1B (human homolog SERPINA1), SERPINA1D (human homolog SERPINA1), and SERPIND1 were even more significantly down-regulated than SERPINC1 (Supplementary Fig. 16b), representing potentially more impactful targets for mitigating ASNase-induced VTE. Although no recombinant variants of PLG or SERPIND1 exist yet, INBRX-101, a recombinant Fc fusion protein of SERPINA1 (alpha-1 antitrypsin) is entering Phase 2/3 testing[51]. Given that only 60% of patients with VTE respond to SERPINC1 repletion, our results provide a rationale for testing INBRX-101 for further mitigation of ASNase-induced VTE. Overall, our data confirm previous findings and identify additional changes in complement and coagulation cascade proteins following ASNase treatment and identify key organ sites that may drive the observed effects.

Within the 17 down-regulated proteins in the cholesterol metabolism pathway, 6 (APOA1, APOA2, APOA4, APOC2, LCAT, and SORT1) are negative modulators of triglyceride levels, and their down-regulation potentially explains ASNase-induced hypertriglyceridemia[52,53]. It has been hypothesized that ASNase-induced hypertriglyceridemia, which occurs in up to 50% of patients, is the result of very low-density lipoprotein (VLDL) up-regulation[52,54]. That hypothesis is not sufficiently granular, though, because VLDL components can be positive or negative modulators of triglyceride levels based on whether they facilitate secretion or uptake of triglycerides. Considering VLDL components as a whole, our data revealed prominent down-regulation of APOA4, APOC1, APOC2, APOE, and APOH in SQWAT, lung, liver, large intestine, and heart tissues (Fig. 5e, Fig. 6a, c, and Supplementary Fig. 16c). All of those except APOE are negative modulators of triglyceride levels; their down-regulation could potentially explain ASNase-induced hypertriglyceridemia. In four tissues we also observed a notable increase in adiponectin (ADIPOQ), which promotes the catabolism of VLDL triglycerides and may explain the observed down-regulation of VLDL apolipoproteins (Fig. 6b)[55]. Together, these findings support the following mechanistic hypothesis to explain ASNase-induced hypertriglyceridemia: (i) nutrient stress triggers lipogenic processes culminating in triglyceride synthesis; (ii) ASNase suppresses the capacity of organs (primarily the liver) to assemble triglyceride-VLDL complexes, and/or ASNase-induced ADIPOQ rapidly catabolizes such complexes before they can be exported; and (iii) free triglycerides are secreted into systemic circulation without a mechanism to distribute them into tissues (mainly fat), leading to triglyceride accumulation in the blood.

In considering therapeutic strategies to mitigate ASNase-induced hypertriglyceridemia, our results identify ADIPOQ as one potential target, but no inhibitors are currently available. Additional candidate targets include the two known positive modulators of triglyceride levels—APOC3 and APOE. Indeed, our data indicates that APOC3 was maintained near baseline levels or elevated in SQWAT, spleen, stomach, large intestine, kidney, muscle, brain, and bone marrow (Fig. 6a). APOC3 was recently identified as a target for lowering triglycerides by up to 77% using the antisense inhibitor volanesorsen[56]. APOE, as noted previously, was down-regulated in most tissues, but it was strikingly up-regulated in the small intestine by ASNase. Since APOE-targeted drugs (pioglitazone, rosiglitazone) are available, our findings provide a rationale for testing these and volanesorsen for mitigation of ASNase-induced hypertriglyceridemia.

Insights regarding ASNase efficacy suggested that the spleen and kidney may represent targetable organ vulnerabilities. In response to $ASNase^{WT}$ treatment, spleen exhibited suppression of ASNS, suppressed glutamine metabolism including ASP production, impaired DNA replication, and induction of ferroptosis. Those observations prompt the hypothesis that ASNase may be effective against a broad range of hematological-related malignancies. Although kidney exhibited up-regulation of ASNS, it remains a potential target due to broad suppression of glutamine metabolism induced by $ASNase^{WT}$ treatment. Future work will be required to test the hypothesis that ASNase is effective for treating renal cancers.

Insights regarding ASNase resistance identified system-wide up-regulation of ASNS as a key resistance factor, building upon the reported association between the tumor microenvironment and ASNase resistance[28,38]. The observed up-regulation of liver protein synthesis may also contribute to ASNase resistance. Importantly, our findings explain how low-ASNS tumors can still be resistant to ASNase; if ASNase dosage is insufficient to maintain durable depletion of ASN, tumor proliferation can continue. Because virtually every organ throughout the body up-regulates ASNS to produce ASN following ASNase treatment, the battle between the drug and the body can only be won if ASN depletion is sustained. These findings highlight the critical need for therapeutic drug monitoring protocols focused on ASN measurement in whole blood, rather than relying on methods that measure only enzyme activity levels.

A recent study raised the possibility that the differential anticancer effects observed between ASNaseWT and ASNaseQ59L may be attributable to a higher Km of the Q59L variant for ASN, irrespective of its glutaminase activity[30,57]. Our current analyses show that both ASNaseWT and ASNaseQ59L elicit widespread ASNS upregulation across multiple tissues, prompting the hypothesis that the rate of ASN synthesis may approach or exceed the catalytic capacity of ASNaseQ59L. Taken together, our findings support an ASNase resistance model in which both host-driven adaptive responses and intrinsic enzymatic properties contribute to the observed pharmacodynamic differences. Future work incorporating direct kinetic measurements will be important to delineate the relative impact of enzyme- and host-mediated resistance mechanisms.

The use of ASNS as a predictive biomarker of response to ASNase therapy presents complex considerations. Our findings indicate that ASNase suppresses ASNS up-regulation in selected tissue types, and tumors that exhibit that phenotype are likely to respond well to ASNase. However, because most tissue types exhibit significant up-regulation of ASNS in response to ASNase treatment, tumor-specific ASNS expression may play a relatively minor role in ASNase resistance. Until further clarity is achieved, efforts to extend ASNase therapy to indications should continue to prioritize testing against tumors with low ASNS expression.

Finally, we hasten to emphasize that integrated analysis of amino acids—particularly ASN, ASP, GLU, and GLN—and their associated proteins proved to be particularly valuable for characterizing organ-level nutrient dependencies[58]. To further extend our findings, we performed integrative pathway enrichment of the differential proteins and metabolites across tissues. This multi-omic analysis revealed co-regulation of several metabolic pathways, with pyrimidine metabolism, purine metabolism, and glutathione metabolism most prominently enriched in spleen following ASNase_WT treatment (Supplementary Fig. 23a, Supplementary Data 28). Notably, glutathione metabolism was consistently altered across multiple tissues, particularly spleen and liver, aligning with our proteomic evidence of impaired redox homeostasis (Supplementary Fig. 23b). Network analysis further highlighted glutathione as a central hub linking dysregulated proteins and metabolites, reinforcing its role as a key mediator of ASNase anticancer activity and potentially also its toxicity (Supplementary Fig. 23c). These integrative analyses provide a systems-level view of ASNase action and underscore glutathione metabolism as a focal point for future mechanistic and translational studies.

The in vivo experiments suggest that ASNase treatment may be associated with lipid peroxidation, suggesting potential strategies to mitigate toxicity, such as antioxidant approaches. Moreover, lipid peroxidation markers may serve as early indicators of toxicity risk. Although further preclinical and clinical studies are required, these

results provide a framework for therapeutic development and patient management. As an MS-based proteomics study, the validation experiments included here are intended as illustrative rather than comprehensive, reflecting the method-focused scope of the study. The causal relevance of broader tissue- and pathway-level proteomic changes remains to be explored and warrants further investigation.

While this study focused on total proteome changes to establish a scalable, high-throughput multi-organ workflow, post-translational modifications (PTMs) such as phosphorylation and acetylation are also likely to contribute significantly to ASNase-induced responses. Future extensions incorporating PTM-enrichment strategies will be important to reveal regulatory mechanisms beyond protein abundance and to further integrate proteomic and metabolomic layers for deeper mechanistic insight.

In summary, high-throughput, quantitative proteome profiling enabled deep analysis of the systems pharmacology of ASNase, facilitating the generation of insights into the enzyme-drug's efficacy and toxicity. This work highlights the transformative potential of nDIA-based high-throughput proteomics and demonstrates its applicability to a broad range of life science investigations, including the systems biology of dietary interventions, exercise interventions, environmental factors, genetics, and beyond.

Methods

Materials

Water (LC–MS grade, Optima, Cat. No. 10509404), acetonitrile (LC–MS grade, Optima, Cat. No. 10001334), and formic acid (LC–MS grade, Thermo Scientific Pierce, Cat. No. 13454279) were purchased from Fisher Chemicals. HeLa protein digest standard (Thermo Scientific Pierce, Cat. No. 88328) and yeast digest standard (Thermo Scientific Pierce, Cat. No. A47951) were purchased from Thermo Scientific. MassPREP E. coli digest standard (Cat. No. 186003196) was purchased from Waters. Sequence grade trypsin (Cat. No. V5113) were purchased from Promega.

Mouse treatment and tissue preparation

All animal experiments were approved by the MD Anderson Cancer Center Institutional Animal Care and Use Committee (IACUC) under protocol number 00001658-RN02 and were conducted in accordance with institutional and national guidelines for the care and use of laboratory animals. Male NSG mice (NOD.Cg-Prkdc(scid) IL2rg(tm1Wjl) SzJ) mice were obtained from The Jackson Laboratory (stock no. 005557) and used at 8–10 weeks of age. Mice were housed under specific pathogen–free conditions with a 12 h light/12 h dark cycle, at an ambient temperature of 20–24 °C and relative humidity of 40–60%. NSG mice were treated with PBS (vehicle), 20,000 U/kg $ASNase^{WT}$ (Spectrila®) qd for 8 d, or 20,000 U/kg $ASNase^{Q59L}$ qd for 8 d. We previously found the selected doses of $ASNase^{WT}$ and $ASNase^{Q59L}$ to be curative and ineffective, respectively, against a mouse model of ALL[31]. *Escherichia coli* L-asparaginase II (ASNase) recombinant proteins were produced as described previously[30,31]. Treatments were administered intraperitoneally (IP) immediately above the hind leg. Treatment volume was 0.1 mL. Prior to tissue collection, each mouse was euthanized using a CO_2 chamber. The abdominal cavity was opened and perfused with 50 mL pre-cooled phosphate buffered saline. A total of 507 organs were dissected, snap-frozen in liquid nitrogen, and stored at −80 °C. For each time-point (0, 1, 3, 5, and 8 days), three independent biological replicates per group of mice were treated daily with either drug or vehicle. At each endpoint, tissues were collected from three mice per group. As such, comparisons between drug- and vehicle-treated groups were performed independently at each time point.

Protein extraction and digestion

10 mg of each tissue sample was resuspended in ice-cold protein extraction buffer containing 4 M urea and 50 mM NH_4HCO_3. Homogenization was performed using a ceramic bead kit (Bertin Technologies Cat. No.CK28-R) with an automated homogenizer (Precellys 24 with Cryolys adapter, Bertin Technologies) with 2 × 10 s pulses at 5000 rpm. Homogenates were clarified by centrifugation for 10 min at 10,000 × *g* at 4 °C, and protein concentration was determined by the BCA method. Proteins in the solution were denatured by boiling at 95 °C for 5 min.

For standard sample preparation workflow, 20 μg protein was diluted to 50 μL with 50 mM NH_4HCO_3. Samples were digested by adding 1 μL 400 ng/μL trypsin (Promega) and incubated at 37 °C overnight unless otherwise specified. Samples were acidified with formic acid at ~0.1% (v/v) final concentration by adding 0.5 μL 10% formic acid in water and centrifuged at 10,000 × *g* for 10 min at 4 °C. The supernatant was desalted using BioPureSPN Mini PROTO 300 C18 column (The Nest Group, Cat. No. HUM S18V), dried in vacuum and stored at −80 °C until analysis.

For high-throughput sample preparation method, 20 μg of protein samples were diluted to 50 μL by adding 50 mM NH4HCO3 in the 96 AFA-TUBE TPX plate (Covaris, Cat. No. 520291) and then add 1 μL 400 ng/μL trypsin (Promega). The sample solutions were incubated with sonication at 37 °C for 4 h using R230 Focused-Ultrasonicator (Covaris, Cat. No. 500620). Digested samples in 96-well plates were acidified with formic acid at ~1% (v/v) final concentration by adding 0.5 μL 10% formic acid in water and transferred to Evotip Pure 96-tip racks (Evosep, Cat. No. EV2013) for desalting. The desalted peptide samples were transferred to the Thermo Scientific™ SureSTART™ Level 2 WebSeal™ 96-Well Microtiter Plates (Thermo Scientific, Cat. No. 60180-P210B), dried in vacuum and stored at −80 °C until analysis.

LC–MS/MS analysis

LC–MS/MS analysis were performed using Orbitrap Astral mass spectrometer coupled with Vanquish Neo UHPLC system (Thermo Fisher Scientific). The vacuum dried peptide samples were resuspended with 0.1% of formic acid. Peptides were separated using an Evosep endurance column (Evosep, Cat. No. EV1107, 150 μm × 4 cm) at a flow rate of 5 μL/min. Peptides were chromatographically separated using a linear gradient of solvent B (0.1% formic acid in ACN) and solvent A (0.1% formic acid in water). Linear gradients were as follows: from 10% to 38% of solvent B 1.8 min, 38% to 100% of solvent B from 1.8 to 1.9 min, 100% B from 1.9 to 2 min. For the original DIA method on the Orbitrap Astral MS, MS1 spectra were collected in the Orbitrap every 0.6 s at a resolution of 240,000. The full scan range was 380–980 m/z unless otherwise specified. The MS1 normalized AGC target was set to 500% with a maximum injection time of 5 ms. DIA MS2 scans were acquired in the Astral analyzer over a range of 380–980 m/z with a normalized AGC target of 500% and a maximum injection time of 3.5 ms and an HCD collision energy setting of 25%. Window placement optimization was turned on. The isolation window was set at 2 Th without window overlap. For the optimized DIA method, scan range was changed to 495–745 m/z. Isolation window was set at 1 Th without window overlap. The maximum injection time of MS2 was set at 2.5 ms.

MS data analysis

Raw files from DIA experiments were analyzed in DIA-NN 1.8.1[8]. The spectral library was generated from a mouse reference database (UniProt 2024 release, 21,709 sequences) allowing N-term M excision and 1 missed cleavage. The DIA-NN search included the following settings: Protein inference = "Genes", Neural network classifier = " Single-pass mode", Quantification strategy = "Robust LC (high precision)", Cross-run normalization = "RT-dependent", Library Generation = "Smart Profiling" and Speed and RAM usage = "Optimal results". Mass accuracy and MS1 accuracy were set to 0 for automatic inference. "No share spectra", "Heuristic protein inference" and "MBR" were checked. The output results from DIA-NN were filtered for Q.Value

≤0.01 and PG.Qvalue ≤0.01. DIA-NN R package was used for protein quantitation using MaxLFQ algorithm.

Differential expression analysis was performed using a two-sample *t*-test comparing group means ($n = 3$ per group). Proteins with a fold change ≥2 or ≤0.5 and an unadjusted $p < 0.05$ were considered differentially expressed, consistent with common practice in proteomics workflows with limited replicates.

To account for multiple hypothesis testing, Benjamini-Hochberg (BH) correction was applied to the raw p values to estimate the false discovery rate (FDR). Adjusted p-values are provided in Supplementary Data 10 for transparency. Due to the limited sample size, the adjusted p values were overly conservative and identified few (if any) significant proteins under FDR < 0.05, a known limitation in small-scale proteomics datasets. Therefore, results discussed in the main text are based on the raw p value threshold combined with fold change filtering.

Analysis of metabolites

Metabolites profiling was conducted on snap-frozen tissue samples by ultra-high-resolution MS. Approximately 20–30 mg of each sample was pulverized in liquid nitrogen and then homogenized with Precellys Tissue Homogenizer.

Metabolites were extracted using ice-cold 0.1% ammonium hydroxide in an 80/20 (v/v) methanol/water solution. The extracts were then centrifuged at 17,000 × *g* for 5 min at 4 °C, and the supernatants were transferred to clean tubes. The solvents were evaporated under nitrogen to dryness. The dried extracts were reconstituted in deionized water, and 5 µL was injected for analysis by ion chromatography (IC)-MS. IC mobile phase A (MPA) was water, and mobile phase B (MPB) was water containing 100 mM KOH. The analysis was performed using a Thermo Scientific Dionex ICS-5000+ capillary IC system with a Thermo IonPac AS11 column (4 µm particle size, 250 × 2 mm). The column compartment was maintained at 30 °C, and the autosampler tray was kept at 4 °C. The IC flow rate was 350 µL/min with the following gradient conditions: starting at 1 mM KOH, increasing to 35 mM over 25 min, further increasing to 99 mM over 39 min, and holding at 99 mM for 10 min. To enhance desolvation for better sensitivity, methanol was delivered via an external pump and mixed with the post-column eluent using a low dead volume mixing tee. Data acquisition was performed with a Thermo Orbitrap Fusion Tribrid Mass Spectrometer in ESI negative ionization mode with a resolution of 240,000 in data dependent acquisition mode, with scan ranges of 80–800 m/z. An Orbitrap resolution of 240,000 (FWHM) was used for MS1 acquisition and spray voltages of −2800 V was used for negative ionization modes. Vaporizer and ion transfer tube temperatures were set at 400 °C and 350 °C, respectively. The sheath, auxiliary and sweep gas pressures were 35, 10, and 0 (arbitrary units), respectively. For MS2 fragmentation a HCD approach was used with stepped collision energy at 20, 30 and 40%. MS2 fragments were detected using an Orbitrap resolution at 30,000. Raw data files were analyzed using Thermo Trace Finder 4.1 software. Final result is normalized by tissue weight.

For amino acid analysis, samples were extracted using 1 mL of ice-cold 90/10 (v/v) acetonitrile/water containing 0.1% formic acid. The extracts were centrifuged at 17,000 × *g* for 5 min at 4 °C, and the supernatants were transferred to clean tubes. The solvent was evaporated under nitrogen to dryness. The dried extracts were reconstituted in 90/10 acetonitrile/water with 1% formic acid, and 10 µL was injected for analysis by liquid chromatography (LC)-MS. LC mobile phase A (MPA; weak) was acetonitrile containing 1% formic acid, and mobile phase B (MPB; strong) was water containing 50 mM ammonium formate. The analysis was preformed using Thermo Vanquish LC system equipped with an Imtakt Intrada Amino Acid column (3 µm particle size, 150 × 2.1 mm), maintained at 30 °C. The autosampler tray was kept to 4 °C. The flow rate was 300 µL/min. The gradient conditions were as follows: initial 15% MPB, increasing to 30% MPB at 20 min, further increasing to 95% MPB at 30 min, holding at 95% MPB for 10 min, and then returning to the initial conditions for equilibration over 10 min. The total run time was 50 min. A Thermo Fisher Scientific Orbitrap Fusion Tribrid mass spectrometer with heated electrospray ionization source was operated in data dependent acquisition mode, in positive ionization modes, with scan ranges of 70–450 m/z. An Orbitrap resolution of 240,000 (FWHM) was used for MS1 acquisition and spray voltages of 3800 V was used for positive ionization modes. Vaporizer and ion transfer tube temperatures were set at 350 °C and 275 °C, respectively. The sheath, auxiliary and sweep gas pressures were 35, 10, and 0 (arbitrary units), respectively. For MS2 fragmentation a HCD approach was used with stepped collision energy at 20, 30 and 40%. MS2 fragments were detected using an Orbitrap resolution at 30,000. Raw data files were analyzed using Thermo Trace Finder 4.1 software. Final result is normalized by tissue weight. Peaks with a signal-to-noise ratio <3 were considered undetected.

Reporting summary

Further information on research design is available in the Nature Portfolio Reporting Summary linked to this article.

Data availability

All data generated in this study are available in the main text or the supplementary materials. Source data are provided with this paper. The mass spectrometry proteomics data have been deposited to the ProteomeXchange Consortium via the PRIDE partner repository with the dataset identifier PXD055919 (nDIA proteomics method optimization) and PXD055590 (multi-organ proteomics dataset). The complete multi-organ proteomics dataset is also available through an interactive online database: https://bioinformatics.mdanderson.org/public-datasets/supplements/ultra-fast-multi-organ-proteomics. The metabolomic data have been deposited on Metabolomics Workbench under Study ID ST004552 [https://doi.org/10.21228/M8F278]. Supplementary Data 10 is available on Figshare at https://doi.org/10.6084/m9.figshare.31143709. Source data are provided with this paper.

References

1. Werner, H. M. J., Mills, G. B. & Ram, P. T. Cancer systems biology: a peek into the future of patient care? *Nat. Rev. Clin. Oncol.* **11**, 167–176 (2014).
2. Kuenzi, B. M. & Ideker, T. A census of pathway maps in cancer systems biology. *Nat. Rev. Cancer* **20**, 233–246 (2020).
3. Goodwin, S., McPherson, J. D. & McCombie, W. R. Coming of age: ten years of next-generation sequencing technologies. *Nat. Rev. Genet* **17**, 333–351 (2016).
4. Shendure, J. & Ji, H. Next-generation DNA sequencing. *Nat. Biotechnol.* **26**, 1135–1145 (2008).
5. Meissner, F., Geddes-McAlister, J., Mann, M. & Bantscheff, M. The emerging role of mass spectrometry-based proteomics in drug discovery. *Nat. Rev. Drug Discov.* **21**, 637–654 (2022).
6. Aebersold, R. & Mann, M. Mass-spectrometric exploration of proteome structure and function. *Nature* **537**, 347–355 (2016).
7. Bader, J. M., Albrecht, V. & Mann, M. MS-based proteomics of body fluids: the end of the beginning. *Mol. Cell Proteom.* **22**, 100577 (2023).
8. Demichev, V., Messner, C. B., Vernardis, S. I., Lilley, K. S. & Ralser, M. DIA-NN: neural networks and interference correction enable deep proteome coverage in high throughput. *Nat. Methods* **17**, 41–44 (2020).
9. Mann, M., Kumar, C., Zeng, W. F. & Strauss, M. T. Artificial intelligence for proteomics and biomarker discovery. *Cell Syst.* **12**, 759–770 (2021).
10. Gessulat, S. et al. Prosit: proteome-wide prediction of peptide tandem mass spectra by deep learning. *Nat. Methods* **16**, 509–518 (2019).

11. Martinez-Val, A., Bekker-Jensen, D. B., Hogrebe, A. & Olsen, J. V. Data processing and analysis for DIA-based phosphoproteomics using spectronaut. *Proteom. Data Anal.* **2361**, 95–107 (2021).
12. Lou, R. et al. Benchmarking commonly used software suites and analysis workflows for DIA proteomics and phosphoproteomics. *Nat. Commun.* **14**, 94 (2023).
13. Shevchenko, A., Tomas, H., Havlis, J., Olsen, J. V. & Mann, M. In-gel digestion for mass spectrometric characterization of proteins and proteomes. *Nat. Protoc.* **1**, 2856–2860 (2006).
14. Wisniewski, J. R., Zougman, A., Nagaraj, N. & Mann, M. Universal sample preparation method for proteome analysis. *Nat. Methods* **6**, 359–362 (2009).
15. Adachi, J. et al. Improved proteome and phosphoproteome analysis on a cation exchanger by a combined acid and salt gradient. *Anal. Chem.* **88**, 7899–7903 (2016).
16. Wang, Y. et al. Reversed-phase chromatography with multiple fraction concatenation strategy for proteome profiling of human MCF10A cells. *Proteomics* **11**, 2019–2026 (2011).
17. Horie, K. et al. Hydrophilic interaction chromatography using a meter-scale monolithic silica capillary column for proteomics LC-MS. *Anal. Chem.* **86**, 3817–3824 (2014).
18. Guzman, U. H. et al. Ultra-fast label-free quantification and comprehensive proteome coverage with narrow-window data-independent acquisition. *Nat. Biotechnol.* **42**, 1855–1866 (2024).
19. Stewart, H. I. et al. Parallelized acquisition of orbitrap and astral analyzers enables high-throughput quantitative analysis. *Anal. Chem.* **95**, 15656–15664 (2023).
20. Heil, L. R. et al. Evaluating the performance of the astral mass analyzer for quantitative proteomics using data-independent acquisition. *J. Proteome Res.* **22**, 3290–3300 (2023).
21. Serrano, L. R. et al. The one hour human proteome. *Mol. Cell Proteom.* **23**, 100760 (2024).
22. Messner, C. B. et al. Ultra-fast proteomics with Scanning SWATH. *Nat. Biotechnol.* **39**, 846–854 (2021).
23. Szyrwiel, L., Gille, C., Mulleder, M., Demichev, V. & Ralser, M. Fast proteomics with dia-PASEF and analytical flow-rate chromatography. *Proteomics* **24**, e2300100 (2024).
24. Ishikawa, M. et al. Optimization of ultrafast proteomics using an LC-quadrupole-orbitrap mass spectrometer with data-independent acquisition. *J. Proteome Res.* **21**, 2085–2093 (2022).
25. Muller, T. et al. Automated sample preparation with SP3 for low-input clinical proteomics. *Mol. Syst. Biol.* **16**, e9111 (2020).
26. Leutert, M., Rodriguez-Mias, R. A., Fukuda, N. K. & Villen, J. R2-P2 rapid-robotic phosphoproteomics enables multidimensional cell signaling studies. *Mol. Syst. Biol.* **15**, e9021 (2019).
27. Kverneland, A. H. et al. Fully automated workflow for integrated sample digestion and evotip loading enabling high-throughput clinical proteomics. *Mol. Cell Proteom.* **23**, 100790 (2024).
28. Van Trimpont, M. et al. Novel insights on the use of L-asparaginase as an efficient and safe anti-cancer therapy. *Cancers* **14**, 902 (2022).
29. Nguyen, H. A., Su, Y. & Lavie, A. Design and characterization of Erwinia chrysanthemi L-asparaginase variants with diminished L-glutaminase activity. *J. Biol. Chem.* **291**, 17664–17676 (2016).
30. Chan, W. K. et al. The glutaminase activity of L-asparaginase is not required for anticancer activity against ASNS-negative cells. *Blood* **123**, 3596–3606 (2014).
31. Chan, W. K. et al. Glutaminase activity of L-asparaginase contributes to durable preclinical activity against acute lymphoblastic leukemia. *Mol. Cancer Ther.* **18**, 1587–1592 (2019).
32. Horvath, T. D. et al. Assessment of l-asparaginase pharmacodynamics in mouse models of cancer. *Metabolites* **9**, 10 (2019).
33. Blachier, J. et al. L-asparaginase anti-tumor activity in pancreatic cancer is dependent on its glutaminase activity and resistance is mediated by glutamine synthetase. *Exp. Cell Res.* **426**, 113568 (2023).
34. Pathria, G., Verma, S., Yin, J., Scott, D. A. & Ronai, Z. A. MAPK signaling regulates c-MYC for melanoma cell adaptation to asparagine restriction. *EMBO Rep.* **22**, e51436 (2021).
35. Lorenzi, P. L. et al. Asparagine synthetase as a causal, predictive biomarker for L-asparaginase activity in ovarian cancer cells. *Mol. Cancer Ther.* **5**, 2613–2623 (2006).
36. Lorenzi, P. L. et al. Asparagine synthetase is a predictive biomarker of L-asparaginase activity in ovarian cancer cell lines. *Mol. Cancer Ther.* **7**, 3123–3128 (2008).
37. Apfel, V. et al. Therapeutic assessment of targeting ASNS combined with l-asparaginase treatment in solid tumors and investigation of resistance mechanisms. *ACS Pharm. Transl. Sci.* **4**, 327–337 (2021).
38. Grima-Reyes, M. et al. Tumoral microenvironment prevents de novo asparagine biosynthesis in B cell lymphoma, regardless of ASNS expression. *Sci. Adv.* **8**, eabn6491 (2022).
39. Kanehisa, M. S. Goto, KEGG: kyoto encyclopedia of genes and genomes. *Nucleic Acids Res* **28**, 27–30 (2000).
40. Yu, M. et al. L-asparaginase inhibits invasive and angiogenic activity and induces autophagy in ovarian cancer. *J. Cell. Mol. Med.* **16**, 2369–2378 (2012).
41. Higuchi-Sanabria, R. et al. Lysosomal recycling of amino acids affects ER quality control. *Sci. Adv.* **6**, eaaz9805 (2020).
42. Dixon, S. J. & Pratt, D. A. Ferroptosis: a flexible constellation of related biochemical mechanisms. *Mol. Cell* **83**, 1030–1042 (2023).
43. Sullivan, L. B. et al. Supporting aspartate biosynthesis is an essential function of respiration in proliferating cells. *Cell* **162**, 552–563 (2015).
44. Birsoy, K. et al. An essential role of the mitochondrial electron transport chain in cell proliferation is to enable aspartate synthesis. *Cell* **162**, 540–551 (2015).
45. Nikonorova, I. A. et al. Obesity challenges the hepatoprotective function of the integrated stress response to asparaginase exposure in mice. *J. Biol. Chem.* **292**, 6786–6798 (2017).
46. Garcia-Montojo, M. et al. TDP-43 proteinopathy in ALS is triggered by loss of ASRGL1 and associated with HML-2 expression. *Nat. Commun.* **15**, 4163 (2024).
47. Heurich, M. & McCluskey, G. Complement and coagulation cross-talk—factor H in the spotlight. *Immunobiology* **228**, 152707 (2023).
48. Priest, J. R., Ramsay, N. K., Bennett, A. J., Krivit, W. & Edson, J. R. The effect of L-asparaginase on antithrombin, plasminogen, and plasma coagulation during therapy for acute lymphoblastic leukemia. *J. Pediatr.* **100**, 990–995 (1982).
49. Goyal, G. & Bhatt, V. R. L-asparaginase and venous thromboembolism in acute lymphocytic leukemia. *Future Oncol.* **11**, 2459–2470 (2015).
50. Zwicker, J. I. et al. The prevention and management of asparaginase-related venous thromboembolism in adults: guidance from the SSC on Hemostasis and Malignancy of the ISTH. *J. Thromb. Haemost.* **18**, 278–284 (2020).
51. Brantly, M. L. et al. Recombinant alpha-1 antitrypsin-Fc fusion protein INBRX-101 in adults with alpha-1 antitrypsin deficiency: a phase 1 study. *Chronic Obstr. Pulm. Dis.* **11**, 282–292 (2024).
52. Parsons, S. K. et al. Asparaginase-associated lipid abnormalities in children with acute lymphoblastic leukemia. *Blood* **89**, 1886–1895 (1997).
53. Juluri, K. R., Siu, C. & Cassaday, R. D. Asparaginase in the treatment of acute lymphoblastic leukemia in adults: current evidence and place in therapy. *Blood Lymphat. Cancer* **12**, 55–79 (2022).
54. Schmiegelow, K., Rank, C. U., Stock, W., Dworkin, E. & van der Sluis, I. SOHO state of the art updates and next questions: management of asparaginase toxicity in adolescents and young adults with acute lymphoblastic leukemia. *Clin. Lymphoma Myeloma Leuk.* **21**, 725–733 (2021).
55. Qiao, L., Zou, C., van der Westhuyzen, D. R. & Shao, J. Adiponectin reduces plasma triglyceride by increasing VLDL triglyceride catabolism. *Diabetes* **57**, 1824–1833 (2008).

56. Gagnon, E. & Arsenault, B. J. Drug target Mendelian randomization supports apolipoprotein C3-lowering for lipoprotein-lipid levels reductions and cardiovascular diseases prevention. *Atherosclerosis* **391**, 117501 (2024).
57. Van Trimpont, M. et al. A human-like glutaminase-free asparaginase is highly efficacious in ASNS(low) leukemia and solid cancer mouse xenograft models. *Cancer Lett.* **611**, 217404 (2024).
58. Yoo, Y. A. et al. Asparagine dependency is a targetable metabolic vulnerability in TP53-altered castration-resistant prostate cancer. *Cancer Res.* **84**, 3004–3022 (2024).

Acknowledgements

We thank all members of MD Anderson Proteomics Core Facility and Metabolomics Core Facility for their help and constructive discussions. This work was supported by NIH grant numbers 1S10OD012304-01, P30CA016672, P30CA033572, and The University of Texas MD Anderson Cancer Center. This research was supported in part by the National Cancer Institute of the National Institutes of Health grant number P30CA033572. We acknowledge the Metabolomics Workbench (https://www.metabolomicsworkbench.org, supported by NIH grants U2C-DK119886 and OT2-OD030544) for hosting the data and metadata for this study (Study ID: ST004552).

Author contributions

Y.X., W.K.C., and P.L.L. conceived the project. Y.X. performed all experiments with assistance from L.T., W.K.C., D.Z., H.Z., E.S.Y., S.R.D., J.D., B.W., B.T., S.M., I.M., H.I.S., and D.J.H. L.T., B.T., and S.M. conducted the metabolomics analysis. W.K.C., E.S.Y., and S.R.D. carried out mouse experiments. Y.X. handled data analysis and figure preparation. F.H.W. and R.A. generated online database. Y.X. wrote the manuscript, while P.L.L. and J.N.W. revised it with input from all authors. P.L.L., J.C., and J.N.W. supervised the study.

Competing interests

The authors declare no competing interests.

Additional information

Supplementary information The online version contains supplementary material available at https://doi.org/10.1038/s41467-026-69471-4.

Correspondence and requests for materials should be addressed to Philip L. Lorenzi.

Peer review information *Nature Communications* thanks Tiannan Guo, Jeroen Krijgsveld and the other, anonymous, reviewer(s) for their contribution to the peer review of this work. A peer review file is available.